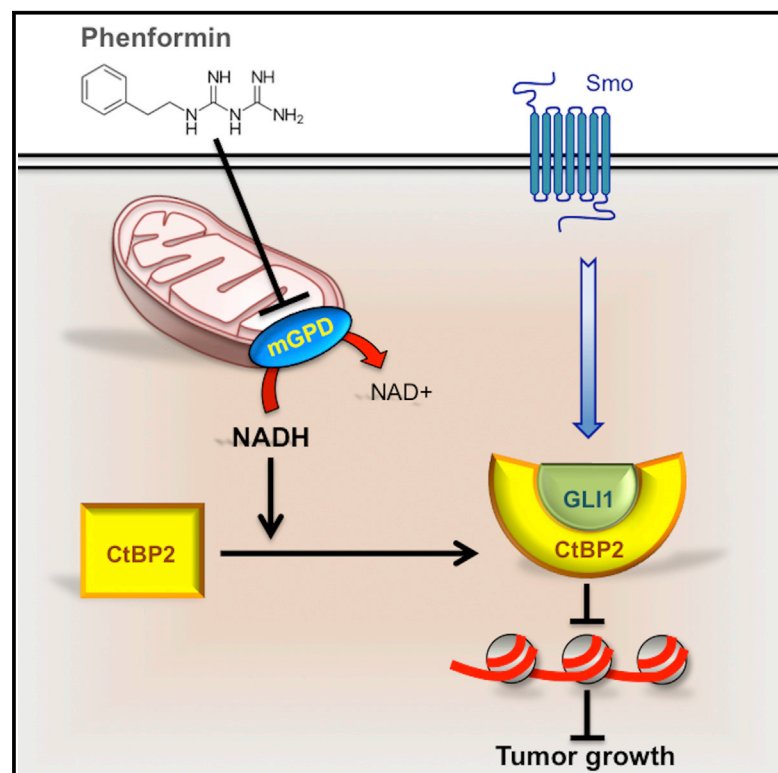# Phenformin Inhibits Hedgehog-Dependent Tumor Growth through a Complex I-Independent Redox/Corepressor Module

Graphical Abstract

Authors

Laura Di Magno, Simona Manni, Fiorella Di Pastena, ..., Enzo Agostinelli, Marella Maroder, Gianluca Canettieri

Correspondence

gianluca.canettieri@uniroma1.it

In Brief

Di Magno et al. investigate the therapeutic properties of phenformin in Hedgehog-dependent tumors. At clinically relevant doses, phenformin works independent of respiratory complex I through mGPD-mediated increase of the redox state. This promotes CtBP2/Gli1 complex formation and consequent inhibition of Hedgehog transcriptional output and tumor growth.

Highlights

- Therapeutic doses of phenformin suppress Hedgehog-dependent tumor growth

- Phenformin inhibits mGPD in cancer cells but does not affect complex I activity

- Inhibition of tumor mGPD mimics phenformin and increases redox state/NADH content

- Elevated NADH promotes Gli1/CtBP2 complex formation and inhibition of tumor growth

CellPress

Phenformin Inhibits Hedgehog-Dependent Tumor Growth through a Complex I-Independent Redox/Corepressor Module

Laura Di Magno,[1,11] Simona Manni,[2,11] Fiorella Di Pastena,[2,11] Sonia Coni,[2] Alberto Macone,[3] Sara Cairoli,[4] Manolo Sambucci,[5] Paola Infante,[1] Marta Moretti,[2] Marialaura Petroni,[2] Carmine Nicoletti,[6] Carlo Capalbo,[2] Enrico De Smaele,[7] Lucia Di Marcotullio,[2,8] Giuseppe Giannini,[2] Luca Battistini,[5] Bianca Maria Goffredo,[4] Egidio Iorio,[9] Enzo Agostinelli,[3,10] Marella Maroder,[2] and Gianluca Canettieri[2,8,10,12,*]

[1]Center for Life Nano Science@Sapienza, Istituto Italiano di Tecnologia, 00161 Rome, Italy
[2]Department of Molecular Medicine, Sapienza University of Rome, 00161 Rome, Italy
[3]Department of Biochemical Sciences A. Rossi Fanelli, Sapienza University of Rome, 00185 Rome, Italy
[4]Division of Metabolism and Research Unit of metabolic Biochemistry, Children's Hospital and Research Institute Bambino Gesù IRCCS, 00146 Rome, Italy
[5]IRCCS Santa Lucia Foundation, Neuroimmunology Unit, 00143 Rome, Italy
[6]Department of Anatomy, Histology, Forensic Medicine and Orthopaedics, Unit of Histology and Medical Embryology, Sapienza University of Rome, 00161 Rome, Italy
[7]Department of Experimental Medicine, Sapienza University of Rome, 00161 Rome, Italy
[8]Istituto Pasteur, Fondazione Cenci-Bolognetti, Sapienza University of Rome, 00161 Rome, Italy
[9]Core Facilities, Istituto Superiore di Sanità, 00161 Rome, Italy
[10]International Polyamines Foundation-ONLUS, 00159 Rome, Italy
[11]These authors contributed equally
[12]Lead Contact
*Correspondence: gianluca.canettieri@uniroma1.it
https://doi.org/10.1016/j.celrep.2020.01.024

SUMMARY

The antidiabetic drug phenformin displays potent anticancer activity in different tumors, but its mechanism of action remains elusive. Using Shh medulloblastoma as model, we show here that at clinically relevant concentrations, phenformin elicits a significant therapeutic effect through a redox-dependent but complex I-independent mechanism. Phenformin inhibits mitochondrial glycerophosphate dehydrogenase (mGPD), a component of the glycerophosphate shuttle, and causes elevations of intracellular NADH content. Inhibition of mGPD mimics phenformin action and promotes an association between corepressor CtBP2 and Gli1, thereby inhibiting Hh transcriptional output and tumor growth. Because ablation of CtBP2 abrogates the therapeutic effect of phenformin in mice, these data illustrate a biguanide-mediated redox/corepressor interplay, which may represent a relevant target for tumor therapy.

INTRODUCTION

The biguanides metformin and phenformin are antidiabetic drugs associated with well-established anticancer properties in preclinical and clinical settings (Pollak, 2013). Metformin is the only biguanide currently approved for the treatment of type 2 diabetes, and it is the most prescribed oral antidiabetic drug worldwide. Phenformin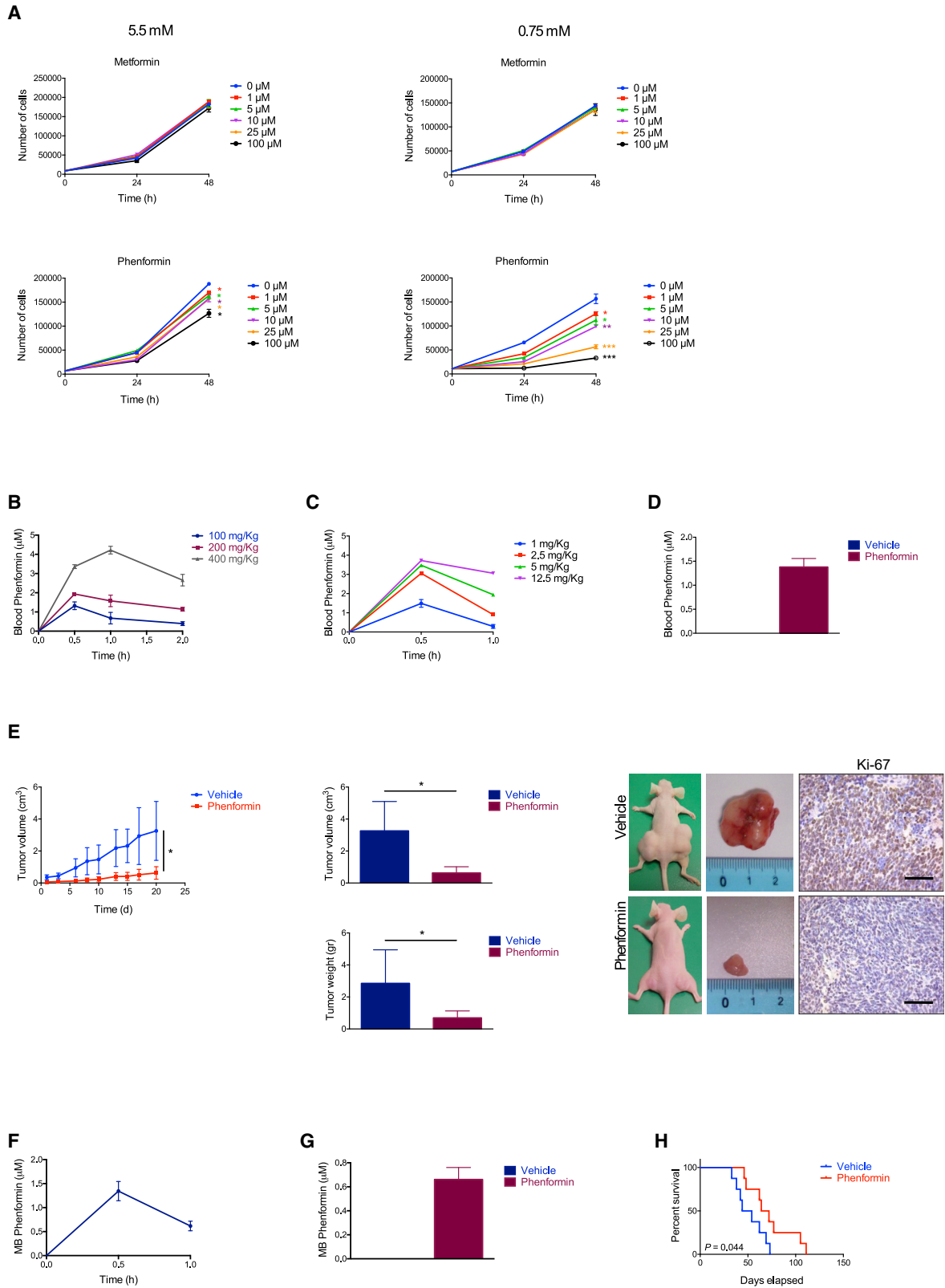 was prescribed for the treatment of diabetes until 1977, and then its use was discontinued because of the relatively more frequent occurrence of lactic acidosis compared with metformin (Berger, 1985). However, studies in the last few years have documented a wider and more pronounced antitumor efficacy of phenformin compared with metformin, renewing interest in this drug (Janzer et al., 2014; Rosilio et al., 2013; Shackelford et al., 2013).

Mechanisms underlying the therapeutic effects of biguanides in diabetes and cancer have been the subject of intense investigation and debate. The most widely accepted model links the effect of these drugs to their ability to inhibit mitochondrial respiratory complex I, thereby inducing an imbalance of the intracellular redox and energetic states and an increase in the NADH/NAD+ and AMP/ATP ratios, respectively (Foretz et al., 2014).

A key target activated by the increase of the AMP/ATP ratio is the energy sensor AMPK, which has been linked to many downstream effects of biguanides in previous studies. It was initially proposed that the glucose-lowering effect of biguanides could be attributed to their ability to activate LKB1/AMPK, thus reducing hepatic glucose production by turning off the transcriptional gluconeogenic program mediated by CRTC2-CREB (Shaw et al., 2005; Zhou et al., 2001). However, it was later discovered that the glucose-lowering effect of metformin is intact in mice lacking AMPK in the liver, raising concerns about the actual relevance of this kinase to the therapeutic response to metformin (Foretz et al., 2010; Miller et al., 2013).

A substantial amount of work has also pointed to AMPK as a key mediator of the direct anticancer properties of biguanides and to AMPK-dependent inhibition of mammalian target of rapamycin (mTOR), which suppresses protein synthesis, cell growth, and viability (Shaw, 2009). In addition, biguanides have been

A

5.5 mM

0.75 mM

Metformin

Metformin

Phenformin

Phenformin

B

C

D

E

Ki-67

Vehicle

Phenformin

F

G

H

(legend on next page)

found to inhibit mTOR activity independent of AMPK via regulation of RAG-guanosine triphosphatase (GTPase) (Kalender et al., 2010).

A crucial concern that has emerged in recent years is that most studies used to elicit the previously described mechanisms employ supra-pharmacological levels of biguanides in the millimolar range. In contrast, oral intake of biguanides in patients results in circulating concentrations within the low micromolar range, 10- to 100-fold lower than those used in cellular studies (He and Wondisford, 2015). For example, the *in vitro* inhibition of complex I requires elevated doses of metformin, in the 1–5 mM range (El-Mir et al., 2000). This suggests that at physiologic doses, alternate targets and cellular events likely contribute to the antitumor effects of biguanides.

Sonic hedgehog (Shh) medulloblastoma (MB) is a pediatric brain tumor characterized by aberrant activation of Shh signaling. This pathway regulates key steps during embryonic and postnatal development and determines stem cell fate in adulthood (Briscoe and Thérond, 2013).

Binding of the Shh ligand to its receptor Patched (Ptch) results in de-repression of the transmembrane transducer Smoothened (Smo). This triggers a signaling cascade involving the cytoplasmic regulator Suppressor of Fused (SuFu) ultimately activating Gli transcription factors (Gli1, Gli2, and Gli3). Gli1, a target of Hedgehog (Hh) signaling, is a powerful transcription factor and oncogene and is upregulated in tumors.

Mutations of genes encoding pathway components (*Ptch*, *Smo*, *SuFu*, and *Gli2*) and causing upregulation of signaling are typically found in the Shh MB subgroup. Hence, Hh inhibitors represent an ideal class of drugs for treatment of this type of malignancy. The only U.S. Food and Drug Administration (FDA)-approved compound, the Smo antagonist vismodegib, has shown limited efficacy in patients due to the occurrence of novel Smo mutations or post-receptor mutations. Therefore, other strategies focused on post-receptor inhibition of Hh (Di Magno et al., 2015) are gaining ground. In this regard, our group and others have observed that AMPK turns off canonical Hh signaling by phosphorylating and inhibiting Gli1 (Di Magno et al., 2016; Li

et al., 2015), leading to the assertion that pharmacological activation of AMPK could represent a promising avenue for inhibiting Hh signaling and counteracting Hh-dependent tumors.

Here we demonstrate a mechanism for phenformin-mediated suppression of tumor growth that is independent of both complex I and AMPK. We show that phenformin inhibits Shh MB tumor growth via an interplay between metabolism and transcriptional repression.

RESULTS

Clinical Doses of Phenformin Elicit a Therapeutic Effect on Hh-Dependent Tumors
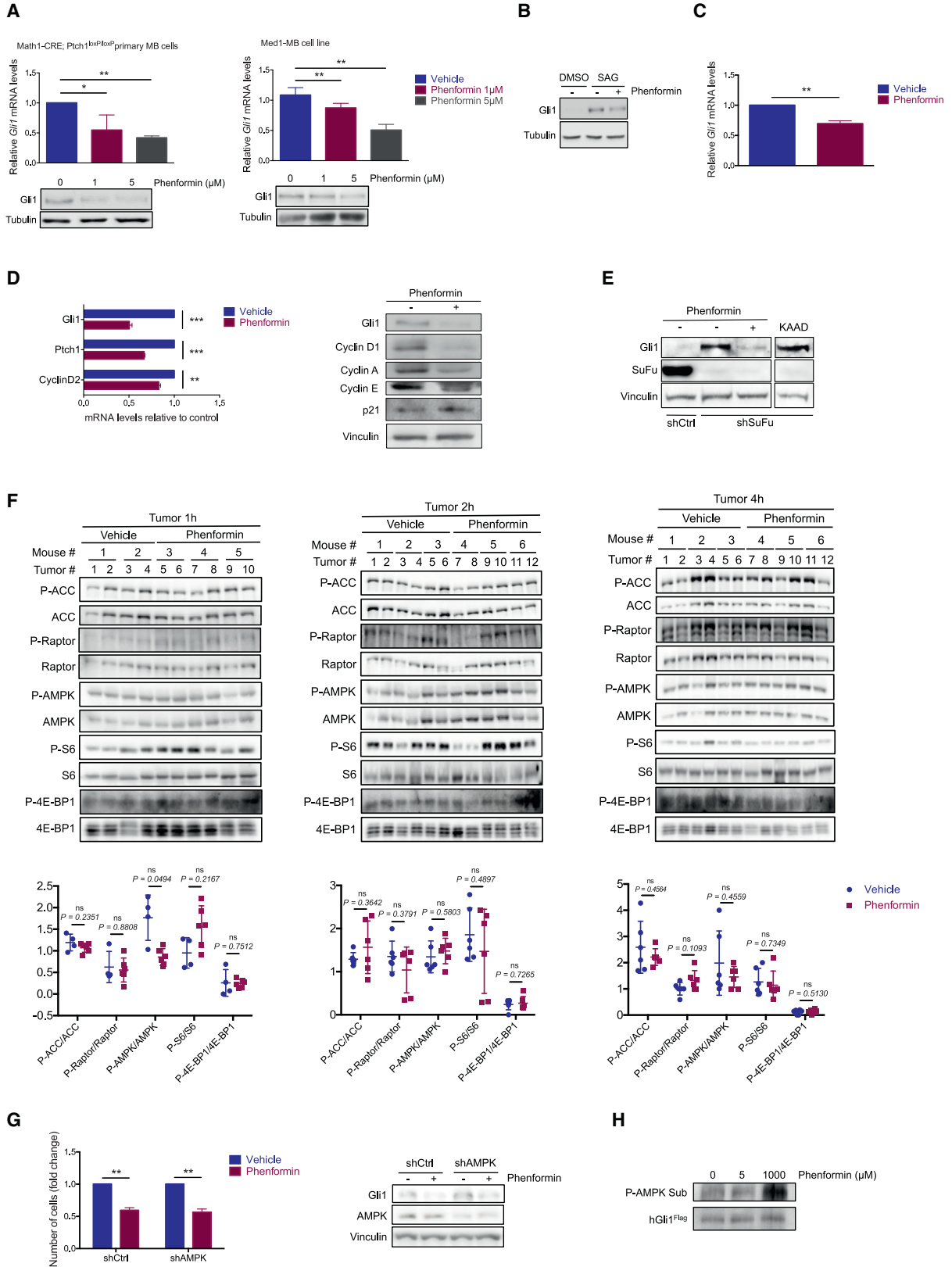
We tested the effect of metformin and phenformin on the growth of Med1-MB cells, a tumor cell line in which developmental Hh signaling is aberrantly activated (Hayden Gephart et al., 2013; Tang et al., 2014; Goodrich et al., 1997). Both biguanides were tested within the micromolar range (1–100 μM) in media containing 5.5 and 0.75 mM glucose, corresponding to the average physiological plasma fasting and estimated cancer tissue glucose concentrations, respectively (Birsoy et al., 2014). To prevent glucose depletion, medium was replaced every 6 h. Exposure of Med1-MB cells to metformin did not cause significant change of tumor growth in either glucose regimen (Figure 1A, top) at any of the concentrations tested, likely a reflection of low levels of metformin OCT1 and OCT3 transporters in these cells, as observed in other tumors (Jackson et al., 2017; Segal et al., 2011). Conversely, the more permeable phenformin induced significant inhibition of cell growth starting from doses as low as 1–5 μM at both glucose concentrations, with a stronger effect at 0.75 mM glucose (Figure 1A, bottom; Figure S1A). Similar data were observed in primary cultures of Shh MB, obtained from Math1-CRE;Ptch1[loxP/loxP] mice (Yang et al., 2008). Micromolar doses of phenformin also caused a reduction of tumor cell growth in this model, confirming the inhibitory effect in cell culture (Figure S1B).

It was previously shown that biguanides inhibit tumor growth in cells with defective mitochondrial function or impaired glucose

---

Figure 1. Phenformin Treatment Inhibits Shh MB Growth at Clinical Concentrations

(A) Med1-MB cells were treated with metformin (top) or phenformin (bottom) at different concentrations, as indicated in the figure, in media containing 5.5 mM (left) or 0.75 mM (right) glucose. Data are representative of three independent experiments, each performed in triplicate.

(B) Blood phenformin levels following oral gavage (o.p.) administration in C57BL/6J mice (n = 6). Blood samples were collected 30 min, 1 h, and 2 h after administration of phenformin (100, 200, and 400 mg/kg, respectively) and analyzed by high-performance liquid chromatography (HPLC).

(C) HPLC analysis of circulating blood plasma phenformin from C57BL/6J mice (n = 4) after tail vein injection, at the indicated concentrations.

(D) HPLC analysis of phenformin in circulating blood plasma from C57BL/6J mice (n = 6). Blood plasma samples were analyzed after 10 days of *ad libitum* administration of phenformin (300 mg/kg/day) in the drinking water. Vehicle, water.

(E) Top, left: growth curves of allograft tumors after injection of primary MB cells from Math1-CRE;Ptch1[loxP/loxP] mice in CD1-nude mice treated with vehicle (water) or phenformin (300 mg/kg/day) *ad libitum per os*. Tumor volume (in cubic centimeters) was measured at the indicated times. Tumor volume (top, middle) and weight (bottom, middle) were measured at the end of the experiment. Right: representative images of allografted mice and isolated tumors at the end of the experiment. Ki-67 staining in excised Med1-MB allograft tumor tissues in phenformin-treated mice or the untreated group is shown. n = 6. Scale bar, 150 μm.

(F) HPLC analysis of phenformin concentration in MB tissues from Math1-CRE;Ptch1[loxP/loxP] mice (n = 4) following i.v. administration of phenformin (12.5 mg/kg) at the indicated time points.

(G) Phenformin concentration in MB tissues derived from Math1-CRE;Ptch1[loxP/loxP] mice (n = 4) treated with vehicle (water) or phenformin (200 mg/kg) for 7 days via o.p., as determined by HPLC.

(H) Kaplan-Meier curve of Math1-CRE;Ptch1[loxP/loxP] mice treated with vehicle (water) (n = 8) or phenformin (300 mg/kg, n = 8) in the drinking water. p = 0.044 as determined by log-rank test.

All data are represented as the mean ± SD of three independent experiments, each performed in triplicate. *p < 0.05, **p < 0.01, ***p < 0.001, by unpaired t test. See also Figure S1.

A

Math1-CRE; Ptch1^loxP/loxP primary MB cells

Med1-MB cell line

B

C

D

E

F

Tumor 1h

Tumor 2h

Tumor 4h

G

H

(legend on next page)

utilization (Birsoy et al., 2014). Thus, we wondered whether our cells were also characterized by any of these defects. Analysis of publicly available gene expression data showed a significant decrease of the glucose utilization signature in Shh MB (Figure S1C). These results were supported by the low levels of glucose transporter GLUT1 and/or of all tested glucose utilization signature genes in primary Shh MB, compared with normal cerebellum, or in Med1-MB cells, compared with tumor cells with intact glucose utilization (Figures S1D and S1E). Altogether, these results suggest that Shh MB and Med1-MB cells have glucose utilization defects.

We next sought to determine the most appropriate concentration of phenformin usage by measuring the plasma levels of the drug in mice (Figure S1F). Similar to a previous report (Bando et al., 2010), we administered increasing amounts of phenformin via oral gavage and measured the blood concentration at various time points. As shown in Figure 1B, the highest concentration detected after 1 h from oral administration of 400 mg/kg of drug did not exceed 5 μM, while higher doses were not tolerated by the animals. Similar results were observed when we administered increasing amounts (1–12.5 mg/kg) of phenformin via tail vein injections (Figure 1C). We also evaluated average circulating concentrations of phenformin reached in a cohort of mice treated with 300 mg/kg/day in the drinking water, corresponding to the maximum administrable dose in this model (Appleyard et al., 2012; Huang et al., 2008). Under these conditions, the plasma concentration of the drug following 10 days of treatment was about 1.4 μM (Figure 1D), which corresponds to the average plasma concentration observed in diabetic patients treated with phenformin (Nattrass et al., 1980). Thus, we established 1–5 μM as the proper therapeutic range (hereafter called the therapeutic dosage) of phenformin concentrations to be used in the subsequent analyses.

We grafted tumor cells from freshly isolated Shh MB, obtained from the Math1-CRE;Ptch1$^{loxP/loxP}$ mice described earlier, into the flanks of immunodeficient athymic nude mice. When the average tumor volume reached 100 mm^3, mice were treated with 300 mg/kg/day phenformin per os (Appleyard et al., 2012), and growth of the tumor masses was measured every 3 days.

Compared with controls, phenformin-treated tumor growth slowed markedly, resulting in a significant decrease in tumor size and weight and of cellular proliferation, as assessed by Ki-67 staining (Figure 1E). To determine the effect of phenformin on spontaneously generated intracranial Shh MB, we measured the intratumor concentrations of the biguanide after oral gavage or intravenous (i.v.) administration in Math1-CRE;Ptch1$^{loxP/loxP}$ mice. In all conditions, the drug was detected in the tumors, reaching a maximum concentration of 1.4 μM within 0.5 h of treatment (Figures 1F and 1G), indicating that the drug crosses the blood-brain barrier (BBB) to access intracranial tumors. We also studied the effect of oral administration of phenformin on overall survival in these mice. Although control littermates had median survival of 49 days from the beginning of the treatment, the survival of mice treated with phenformin was increased by almost 40% (68 days after treatment), indicating the preclinical efficacy of this drug on intracranial, spontaneously generated tumors (Figure 1H).

Phenformin Inhibits Hh Signaling Independent of the Energy-Sensing Machinery

Because aberrant Hh signaling is a key tumorigenic driver in the Shh MB subgroup, we hypothesized that the observed inhibitory effect could result from an inhibition of this pathway. Accordingly, we found that treatment of primary cultures of mouse Shh MB and Med1-MB cells with therapeutic concentrations of phenformin downregulated mRNA levels of Gli1, a well-established Hh target gene (Figure 2A). We also tested the drug on DAOY cells, an Hh-responsive MB cell line (Götschel et al., 2013). Treatment of these cells with the Smoothened agonist (SAG) (Götschel et al., 2013) increased Gli1 levels, and this effect was prevented by the biguanide treatment (Figure 2B). A decrease of *Gli1* mRNA levels was also observed in intracranial

Figure 2. Phenformin Inhibits Hh Signaling Independent of AMP-Mediated Mechanisms

(A) Relative *Gli1* mRNA expression levels in primary tumorspheres derived from Math1-CRE;Ptch1$^{loxP/loxP}$ mice (left) and Med1-MB cells (right) as determined by qPCR. Cells were treated with vehicle (DMEM) or phenformin at the indicated concentrations in media containing 0.75 mM glucose for 48 h. Gli1 protein levels are shown. Tubulin was used as loading control.

(B) Gli1 levels from DAOY cells treated with SAG or DMSO and phenformin (5 μM) for 48 h. Tubulin was used as loading control.

(C) Relative *Gli1* mRNA expression levels in intracranial MB derived from Math1-CRE;Ptch1$^{loxP/loxP}$ mice from Figure 1G. Data were normalized to the expression of *L32 mRNA* and are represented as fold change relative to control (vehicle) sample.

(D) Left: relative expression of *Gli1*, *Ptch1*, and *CyclinD2* mRNA in vehicle-treated (DMEM) or phenformin-treated (5 μM) primary tumorspheres from Math1-CRE;Ptch1$^{loxP/loxP}$ mice, as evaluated by qPCR. Expression levels were normalized to *L32* mRNA and represented as fold change relative to control (vehicle) sample. Right: western blot analysis of the indicated targets in Med1-MB cells after 48 h of treatment with phenformin (5 μM) or vehicle (DMEM). Vinculin was used as loading control.

(E) Western blot analysis of DAOY cells stably transduced with control (shCtrl) or SuFu-specific (shSuFu) shRNAs and treated with phenformin (5 μM) or KAAD-cyclopamine (KAAD, 1 μM) for 48 h. Gli1 and SuFu protein levels are shown. Vinculin was used as loading control. Non-contiguous lanes are indicated.

(F) Western blot analysis of tumor tissues from CD1-nude mice allografted with primary MB cells from Math1-CRE;Ptch1$^{loxP/loxP}$ mice. Mice were treated with phenformin (12.5 mg/kg, i.v.) for 1, 2, and 4 h, and samples were collected at the end of each time point. Lysates were immunoblotted with the indicated antibodies. Densitometric analysis was performed and phosphorylated to total protein ratios calculated.

(G) (Left) Proliferation assay and (right) western blot analysis of Med1-MB cells expressing control (shCtrl) or AMPKα1-specific (shAMPK) shRNAs and treated with phenformin (5 μM) for 48 h. Gli1 and AMPK protein levels are shown. Vinculin was used as loading control.

(H) Gli1 phosphorylation in Med1-MB cells transfected with human FLAG-Gli1 and treated with phenformin at the indicated concentrations for 1 h. After FLAG immunoprecipitation, Gli1 phosphorylation was detected by immunoblotting with anti-phospho serine AMPK substrate antibody.

All data are represented as the mean ± SD of three independent experiments, each performed in triplicate. *p < 0.05, **p < 0.01, ***p < 0.001, ns, not significant, by ANOVA and unpaired t test.

See also Figure S2 and Tables S1 and S2.

Shh MB from Math1-CRE;Ptch1$^{-/-}$ mice treated with phenformin, further demonstrating the ability of the drug to cross the BBB and accumulate to levels sufficient for inhibition of Hh signaling (Figure 2C).

Phenformin also inhibited Ptch1, cyclin D2, cyclin D1, cyclin A, and cyclin E and increased p21 levels, indicating that this drug antagonizes Hh-dependent activation of key cell-cycle targets (Che et al., 2013; Kenney and Rowitch, 2000; Plaisant et al., 2011) at therapeutic doses (Figure 2D).

Next, we examined whether additional tumor types with molecular pathology similar to Shh MB would respond to biguanides. Two additional tumor cell lines were examined: ASZ001 (basal cell carcinoma) and TC71 (Ewing sarcoma), both characterized by aberrant alteration of Hh signaling and upregulation of Gli1 (Aszterbaum et al., 1999; Beauchamp et al., 2009, 2011). Consistent with the results in Shh MB, phenformin inhibited tumor growth and *Gli1* mRNA in both cell types (Figure S2A), suggesting the conservation of the mechanism in tumors dependent on the Hh/Gli pathway.

To establish the molecular mechanism by which phenformin regulates the Hh pathway, we knocked down the cytoplasmic inhibitor SuFu from DAOY cells. As predicted (Gruber et al., 2018), suppression of SuFu augmented Hh transcriptional activity independent of Smo receptor, as evidenced by the increased levels of Gli1 that were not reduced by the Smo inhibitor KAAD-cyclopamine. Conversely, phenformin treatment resulted in significant inhibition of Gli1 protein in SuFu-deficient cells, indicating that the drug acts downstream of Smo, likely by affecting Gli activity (Figure 2E). Studies show that canonical Hh signaling can be inhibited by AMPK-dependent Gli1 phosphorylation (Di Magno et al., 2016; Li et al., 2015). Based on the reported ability of phenformin to activate AMPK, we examined whether our observations of phenformin-dependent suppression of tumor growth could be attributed to this mechanism.

Time-dependent treatment of Med1-MB cells with therapeutic doses of phenformin failed to activate AMPK, as determined by the phosphorylation of T172-AMPK (pAMPK) or phosphorylation of ACC (pACC) and phosphorylation of Raptor (pRaptor), two well-known substrates of AMPK. By contrast, treatment with a higher dose (1 mM) of phenformin robustly increased phosphorylation of all three proteins (Figure S2B). To determine the physiological relevance of this observation, we studied pAMPK, pACC, and pRaptor in tumor tissues from mice treated at various time points (1, 2, and 4 h) with the maximum tolerated dose (12.5 mg/kg) of phenformin (Figure S2C). Supporting the *in vitro* data, AMPK signaling remained unchanged in tumors from phenformin-treated mice compared with mice treated with vehicle (Figure 2F). Similar results were observed in the liver of the same mice (Figure S2D), in keeping with previously published results (Madiraju et al., 2018). Conversely, analysis of AMPK signaling in the lung (the first tissue reached after tail vein injection) showed increased pAMPK and pACC (Figure S2E), according to previous work (Shackelford et al., 2013).

Because biguanides are known to accumulate in the mitochondrial matrix over time, we tested the effect of long-term exposure of the drug. We incubated Med1-MB cells for 2, 6, and 12 days with therapeutic concentrations of phenformin, replacing the drug every day. However, despite these prolonged treatments, phenformin did not change pAMPK and pACC levels, ruling out the possibility of an accumulation-dependent effect on this signaling (Figure S2F).

Consistent with the *in vitro* data, the phosphorylation status of AMPK and its targets in tumor tissues was not modified by chronic oral administration of phenformin in mice (Figure S2G). Altogether, these data demonstrate the absence of phenformin-dependent AMPK signal activation irrespective of time, dose, and/or conditions of treatment.

To further address the involvement of the AMPK-Gli1 axis in the observed effect, we depleted Med1-MB cells of AMPKα1, the only AMPK catalytic isoform expressed in these cells (Figure S2H). The efficacy of knockdown was ascertained by the loss of pACC and pRaptor in AMPK-deficient cells treated with 1 mM phenformin (Figure S2I). As shown in Figure 2G, 5 μM phenformin treatment resulted in inhibition of endogenous Gli1 expression and a decrease in cell proliferation. Both effects were comparable and independent of AMPK expression. Notably, phenformin failed to induce the AMPK-mediated phosphorylation of exogenous Gli1 at the therapeutic doses, an effect that could instead be observed at 1 mM concentration (Figure 2H). Altogether, these data indicate that the inhibitory effect of therapeutic doses of phenformin on Hh signaling and tumor growth is independent of AMPK-mediated inhibition of Gli1.

In most cases, the antitumor properties of biguanides have been attributed to their ability to directly or indirectly inhibit mTOR, a kinase often upregulated in tumors that also modulates Gli activity (Wang et al., 2012). Thus, we investigated the involvement of mTOR by analyzing the phosphorylation levels of its substrates S6 and 4E-BP1 in Med1-MB and in tumor samples of mice (from Figure 1E). Phosphorylation of S6 (pS6) and phosphorylation of 4E-BP1 (p4E-BP1) were not affected by phenformin at the micromolar concentrations in either Shh MB cell lines (Figure S2J) or tumor samples from mice acutely or chronically treated with phenformin (Figure 2F; Figure S2K). However, biguanide treatment reduced pS6 and p4E-BP1 levels at 1 mM (Figure S2J), demonstrating that under therapeutic conditions, phenformin exerts its antitumor effect through mTOR-independent mechanisms.

Because it was found that biguanides also affect protein kinase A (PKA) activity in the liver by depleting AMP and thus cyclic AMP (cAMP) levels (Miller et al., 2013), we also tested the levels of phosphorylated CREB (pCREB), a PKA target that may play a role in tumorigenesis (Steven and Seliger, 2016). Phenformin did not modify pCREB levels at the concentrations tested (Figure S2L).

Altogether, these observations indicate that at the established therapeutic concentrations, phenformin does not affect the previously characterized AMP-dependent targets.

The Antitumor Effect of Phenformin Is Mediated by mGPD-Dependent Changes of the Redox State

Because biguanides are believed to exert most of their actions by inhibiting mitochondrial respiratory complex I (Dykens et al., 2008; El-Mir et al., 2000; Owen et al., 2000), we studied whether, under our experimental conditions, the activity of this complex is affected by the drug. Inhibition of complex I leads to a decrease in oxidative phosphorylation and a concomitant reduction of oxygen consumption and energy balance, with a parallel increase
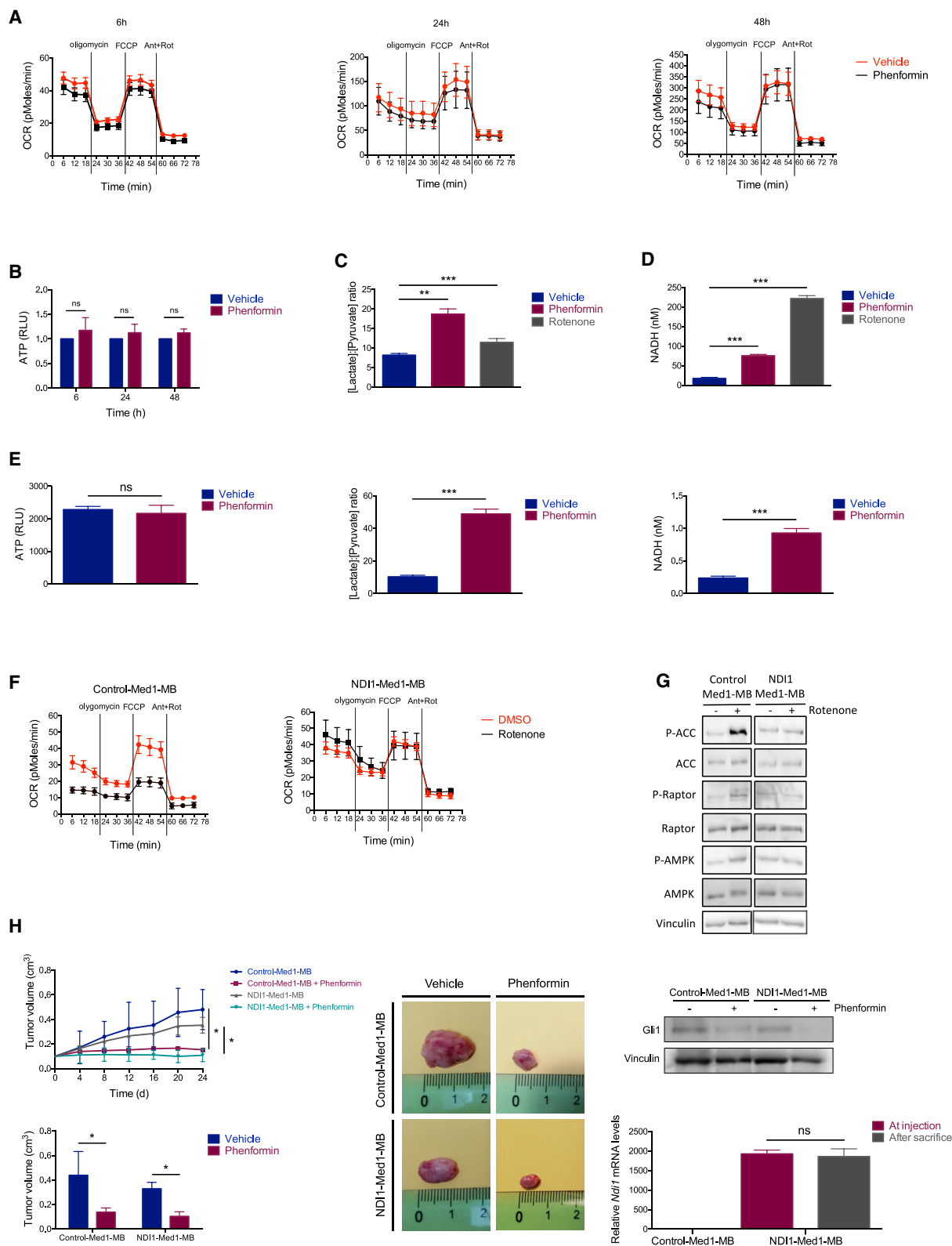
Figure 3. Phenformin Increases the Redox State in Shh MB Cells

(A and B) OCR (A) and ATP (B) content in Med1-MB cells treated with phenformin (5 μM; 6, 24, and 48 h) in media containing 0.75 mM glucose. Results were normalized for protein content. ATP content is expressed as relative luminescence units (RLUs).

(legend continued on next page)

of the redox state, due to the lack of oxidation of the reducing equivalents.

In contrast with this scenario, time-dependent (6, 24, and 48 h) treatment with therapeutic doses of phenformin showed an oxygen consumption rate (OCR) that was not significantly altered (Figure 3A), whereas it was strongly inhibited by the standard complex I inhibitor rotenone or by 1 mM phenformin (Figure S3A). Consistent with these data, ATP content was also not modified by phenformin, while it was significantly reduced by rotenone (Figures 3B; Figure S3B). However, the lactate/pyruvate ratio and the total NADH content were significantly increased in phenformin-treated cells, documenting an increase of the intracellular redox state (Figures 3C and 3D). Similar alterations were observed in mice with allografted (from Figures 1E and 2F) or spontaneously generated Shh MB tumors chronically or acutely treated with phenformin *per os* or i.v. These tumor samples showed a significant increase in the lactate/pyruvate ratio and NADH content, while the ATP levels were unchanged (Figure 3E; Figures S3C and S3D), further indicating the exclusive modification of the redox state in phenformin-treated tumors *in vivo*.

To specifically address the requirement of complex I in this context, we transduced MB cells with retroviruses expressing NDI1, a budding yeast NADH-quinone oxidoreductase. NDI1 transfers electrons from NADH to ubiquinone in the respiratory chain and functionally complements respiratory chain complex I in mammalian cells (Seo et al., 1998), rendering NDI1 cells independent of complex I for respiration and insensitive to rotenone inhibition (Ota et al., 2009; Seo et al., 1999).

Analysis of OCR revealed that NDI1-expressing Med1-MB cells did not show change in basal respiration compared with controls (Figure S3E). Because NDI1 expression increases basal OCR in cells with impaired respiration (Birsoy et al., 2014), these data ruled out mitochondrial dysfunctions in Med1-MB cells.

As expected, rotenone failed to inhibit OCR and ATP production, and no change was observed in pAMPK, pACC, and pRaptor in NDI1-expressing Med1-MB cells (Figures 3F and 3G; Figure S3F). Similarly, supra-physiological (100 μM) doses of phenformin increased pAMPK and its targets in wild-type (WT) cells, but not in NDI1-expressing cells (Figure S3G). Therefore, these experiments confirmed that NDI1-expressing Med1-MB cells are independent from complex I for respiration.

Remarkably, phenformin treatment continued to inhibit tumor growth and expression of Gli1 mRNA in NDI1-expressing MB tumors in mice and in cultured Med1-MB cells (Figure 3H; Figure S3H). In addition, in cells lacking complex I (stably expressing short hairpin RNA [shRNA] against mammalian NDUFS3, a subunit of mammalian complex I) but expressing NDI1, phenformin still inhibited cell growth and Gli1 expression (Figures S3I and S3J), indicating that phenformin displays its antitumor effects in the absence of complex I.

Altogether, these observations demonstrate that phenformin antitumor effects *in vitro* and *in vivo* are independent of complex I in this context and point to an alternative target that alters the redox balance while mediating antitumor properties at therapeutic concentrations of phenformin.

Relevant to this study, a previous report demonstrated that biguanides inhibit enzymatic activity of the mitochondrial glycerophosphate dehydrogenase (mGPD) enzyme, a component of the glycerophosphate shuttle, inhibition of which leads to an increase of the redox state, accumulation of lactate, and suppression of hepatic gluconeogenesis (Madiraju et al., 2014).

We examined whether mGPD was similarly affected in our tumor models, and mGPD activity was assessed in Shh MB tumor extracts treated with phenformin or its corresponding control. In keeping with the previous report, we observed that therapeutic concentrations of phenformin inhibited the activity of immunoaffinity-purified mGPD from Shh MB and liver, as demonstrated by a change in absorbance at 600 nm using 2,6-dichloroindophenol (DCIP) substrate (Figure 4A; Figure S4A). Phenformin treatment also caused an increase of glycerol-3-phosphate (G3P), the mGPD substrate, in MB from Math1-CRE;Ptch1$^{loxP/loxP}$ mice and in Med1-MB cells (Figure 4B; Figures S4B and S4C). Conversely, the complex I inhibitor rotenone failed to induce change in G3P content (Figure 4C), indicating the specificity of the increase of this metabolite in response to mGPD inhibition.

Next, we examined whether direct inhibition of mGPD could reproduce the effect of phenformin in Shh MB cells, using shRNA-mediated lentiviral knockdown of mGPD. Ablation of mGPD caused a significant increase in G3P, the lactate/pyruvate ratio, and NADH (Figure 4D; Figure S4D), indicating that mGPD deficiency mimics the effect of phenformin on the redox balance in tumor cells. In keeping with this finding, ablation of mGPD, but not of the cytoplasmic GPD (cGPD), caused a significant decrease of Med1-MB cell proliferation (Figure 4E; Figure S4E), and cells were refractory to the growth inhibitory effect of phenformin, clearly indicating that mGPD is required for tumor growth and is likely the critical target for phenformin. Supporting our observations that phenformin-mediated inhibition of growth is

(C and D) L-lactate production (C) and NADH (D) content were determined in Med1-MB cells following treatment with phenformin (5 μM) and rotenone (1 μM) for 6 h. L-lactate production is expressed as the lactate/pyruvate ratio.

(E) ATP content (left), L-lactate production (middle), and NADH production (right) in allografted tumors (from Figure 1E), measured at the end of chronic phenformin treatment (300 mg/kg/day, *per os*).

(F and G) OCR (F) and pACC, pRaptor, and pAMPK (G) in Control-Med1-MB and NDI1-Med1-MB cells following treatment with rotenone (40 nM) for 1 h. Vinculin was used as loading control. OCR results were normalized for protein content. Non-contiguous lanes are indicated.

(H) Top, left: growth curves of allograft tumors after injection of Control-Med1-MB and NDI1-Med1-MB cells into the flanks of non-obese diabetic (NOD)/severe combined immunodeficiency (SCID) mice. Mice were treated for 24 days with vehicle (water) or phenformin (300 mg/kg/day) *ad libitum per os*. n = 5. Bottom, left: average tumor volumes (in cubic centimeters). Middle: representative images of excised allografted tumors at the end of the experiment. Top, right: Gli1 protein levels and vinculin (loading control) in tumor lysates. Bottom, right: *Ndi1* mRNA levels of Control-Med1-MB and NDI1-Med1-MB cells at injection into the flanks of NOD/SCID mice and in excised allografted tumors at the end of the experiment. Data were normalized to *L32* mRNA expression levels.

All data are represented as the mean ± SD of three independent experiments, each performed in triplicate. *p < 0.05, **p < 0.01, ***p < 0.001, ns, not significant, by ANOVA and unpaired t test.

See also Figure S3.
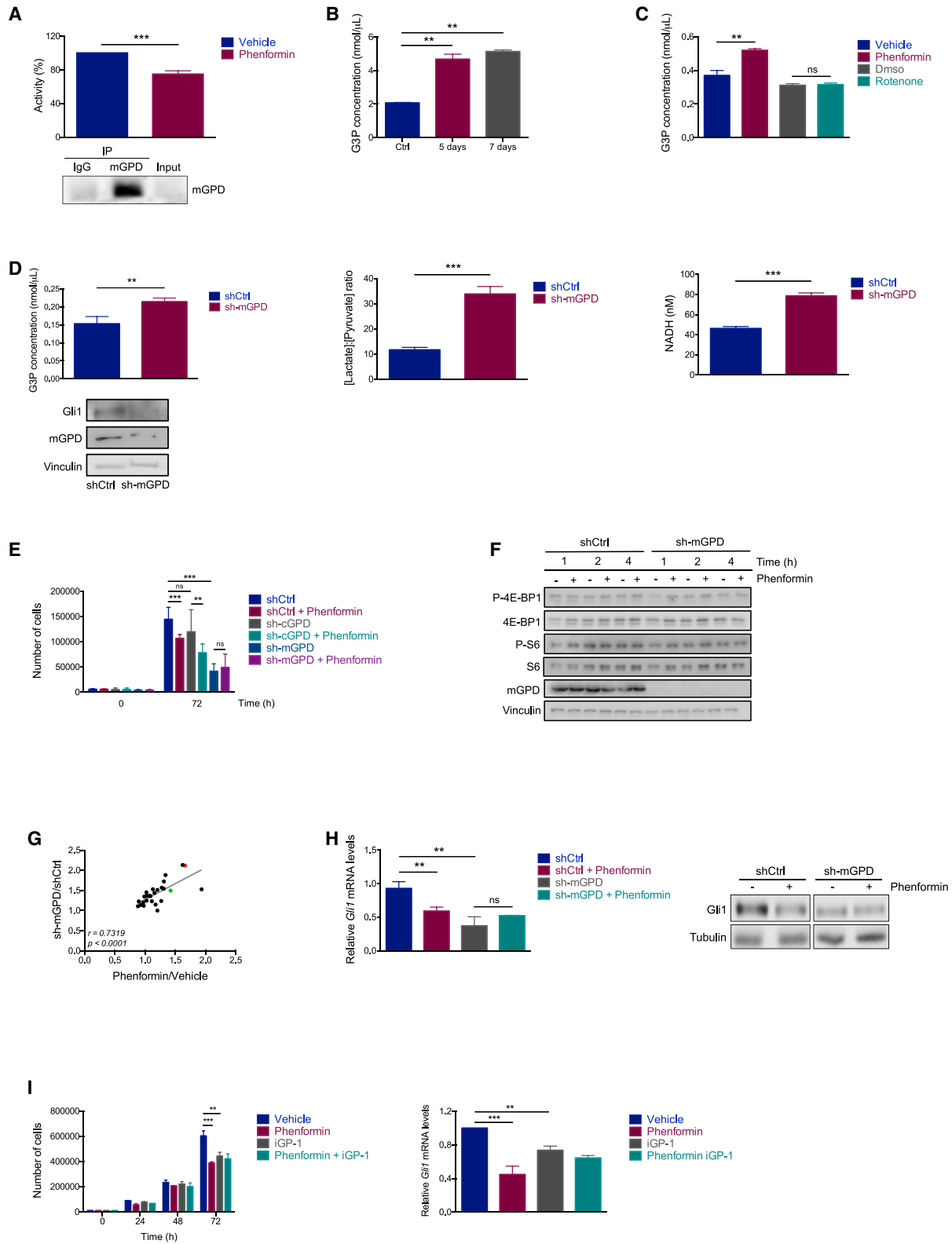
(legend on next page)

independent of mTOR signaling, p4E-BP1 and pS6 levels were not modified by either phenformin or mGPD depletion in MB cells (Figure 4F).

Considering the importance of mGPD in cellular metabolism, we examined whether phenformin treatment or depletion of mGPD altered the metabolic profile of Med1-MB cells using untargeted quantitative ^{1}H-NMR spectroscopy. A total of 27 metabolites were detected, but only a few were significantly changed upon short hairpin mGPD (sh-mGPD) lentiviral knockdown or phenformin treatment. Interestingly, we observed a significant correlation between the two groups (Figure 4G; Figure S4F). Both conditions caused significant elevation of lactate and fumarate, likely a consequence of FAD+ accumulation and due to a block of the glycerophosphate shuttle (see Figure 4D), which correlates with an increase in the redox state. Glutaminolysis metabolites, as well as nucleotides, amino acids, and phospholipid metabolites, was not significantly modified in either group. However, independence from complex I and energy balance was evident by the absence of significant change in the intermediates of the tricarboxylic acid (TCA) cycle, including aspartate, a marker of electron transport chain integrity (Birsoy et al., 2015; Cardaci et al., 2015).

Together with the rest of the data, these overlapping metabolomic profiles of mGPD-depleted and phenformin-treated cells indicate that phenformin mediates its growth inhibitor effects through mGPD inhibition (Figure 4G).

Both mRNA and protein levels of Gli1 were reduced upon knockdown of mGPD, and the lack of mGPD prevented further reduction of Gli1 by phenformin, thereby linking phenformin to Hh-dependent gene expression (Figure 4H) via mGPD. Finally, treatment of MB cells with a selective mGPD agonist, iGP-1 (Orr et al., 2014), resulted in significant inhibition of tumor growth and Hh signaling (Figure 4I), and this effect was not augmented by phenformin cotreatment.

Altogether, these studies provide strong evidence for mGPD as a key target for phenformin-dependent inhibition of tumor growth and Hh signaling.

The NADH-Dependent Transcriptional Corepressor CtBP2 Mediates Phenformin-Induced Hh Inhibition

Having found that mGPD mediates the phenformin effects in tumors by inducing accumulation of NADH, we examined whether such a shift in redox imbalance could drive the inhibition of Hh-dependent gene expression and tumor growth. Because phenformin inhibits Hh-mediated transcription downstream of SuFu, we reasoned that a corepressor with the ability to sense the NADH levels and to inhibit Hh signaling could mediate the observed effect, possibly by associating with Gli.

We hypothesized that the transcriptional repressors C-terminal binding protein 1 and 2 (CtBP1 and CtBP2), which sense and link changes in NADH levels to transcriptional inhibition, may play a role in Gli1-mediated repression of downstream targets (Chinnadurai, 2002).

In coimmunoprecipitation assays, we observed that Gli1 binds to CtBP2, but not CtBP1, in Med1-MB cells (Figure 5A). Conversely, CtBP2 did not associate with Gli2 and Gli3, other two Hh-regulated transcription factors (Figure S5A). Furthermore, phenformin treatment augmented the association between CtBP2 and Gli1 or its well-known partner HDAC2 (Zhao et al., 2006, 2009) (Figure 5B). This increased association was detected after 30 min of phenformin treatment and remained stable for the subsequent time points. The levels of pAMPK and pACC were unchanged under these conditions, confirming the lack of involvement of this signaling in the observed mechanism.

CtBP2 recruitment over the Gli target gene *Ptch1* was also increased (Figure 5C), indicating a drug-induced complex formation at the chromatin level. Supporting the specific ability of CtBP2 to limit Hh activity at a downstream level, ectopic expression of CtBP2 specifically reduced Gli1-responsive reporter activity, an effect abrogated by small interfering RNA (siRNA)-mediated knockdown of Gli1 (Figure 5D).

To prove the functional connection of CtBP2 with mGPD, we used a dual lentivirus-mediated knockdown strategy in Med1-MB cells. Ablation of mGPD caused significant inhibition of cell growth (Figure 5E) and Hh signaling (Figure 5F) that was prevented

---

Figure 4. Inhibition of mGPD Mimics the Phenformin Effect in Tumor Cells

(A) Enzyme assay on mGPD purified from MB mitochondrial lysate derived from Math1-CRE;Ptch1$^{loxP/loxP}$ mice (n = 3). Incubation was performed with or without phenformin (5 μM) in the presence of DCIP as the electron acceptor. Activity was determined as loss of absorbance at 600 nm and expressed as a percentage of control (untreated) sample. Immunoprecipitated levels of mGPD are shown.

(B) G3P levels in MBs from Math1-CRE;Ptch1$^{loxP/loxP}$ mice after long-term phenformin treatment (200 mg/kg/day, o.p.). n = 3.

(C) G3P levels in Med1-MB cells following treatment with phenformin (5 μM) or rotenone (1 μM) for 6 h.

(D) G3P concentration (left), L-lactate production (middle) and NADH content (right) in shControl (shCtrl)-expressing and sh-mGPD-expressing Med1-MB cells. Gli1 and mGPD protein levels are shown. Vinculin was used as loading control.

(E) Proliferation assay on Med1-MB cells expressing shCtrl or cGPD- and mGPD-specific shRNAs and treated with phenformin (5 μM) for 72 h.

(F) Med1-MB cells expressing shCtrl or mGPD-specific shRNAs were treated with phenformin (5 μM) for 1, 2, and 4 h. Lysates were analyzed by immunoblot for the indicated proteins.

(G) Correlation between phenformin-treated and mGPD-knockdown Med1-MB cell metabolites, expressed as the ratio of individual metabolites to all NMR metabolites and normalized to control samples. Spearman's correlation coefficient and significance are shown. Colored dots indicate metabolites with p < 0.05 in both groups (green, L-lactate; red, fumarate).

(H) Expression of *Gli1* mRNA (left) and Gli1 protein levels (right) in vehicle-treated (DMEM) or phenformin-treated (5 μM) Med1-MB cells expressing shCtrl or sh-mGPD as determined by qPCR and western blot. Expression levels were normalized to *L32* mRNA levels, and tubulin levels are shown as control. Non-contiguous lanes are indicated.

(I) Left: proliferation assay on Med1-MB cells treated with phenformin (5 μM) or iGP-1 (100 μM) alone or in combination for the indicated time points. Right: qPCR of the *Gli1* gene in Med1-MB cells collected at the end of the experiment (72 h). mRNA levels were normalized to the expression of *L32*.

All data are represented as the mean ± SD of three independent experiments, each performed in triplicate. **p < 0.01, ***p < 0.001, ns, not significant, by ANOVA and unpaired t test.

See also Figure S4 and Tables S1 and S2.
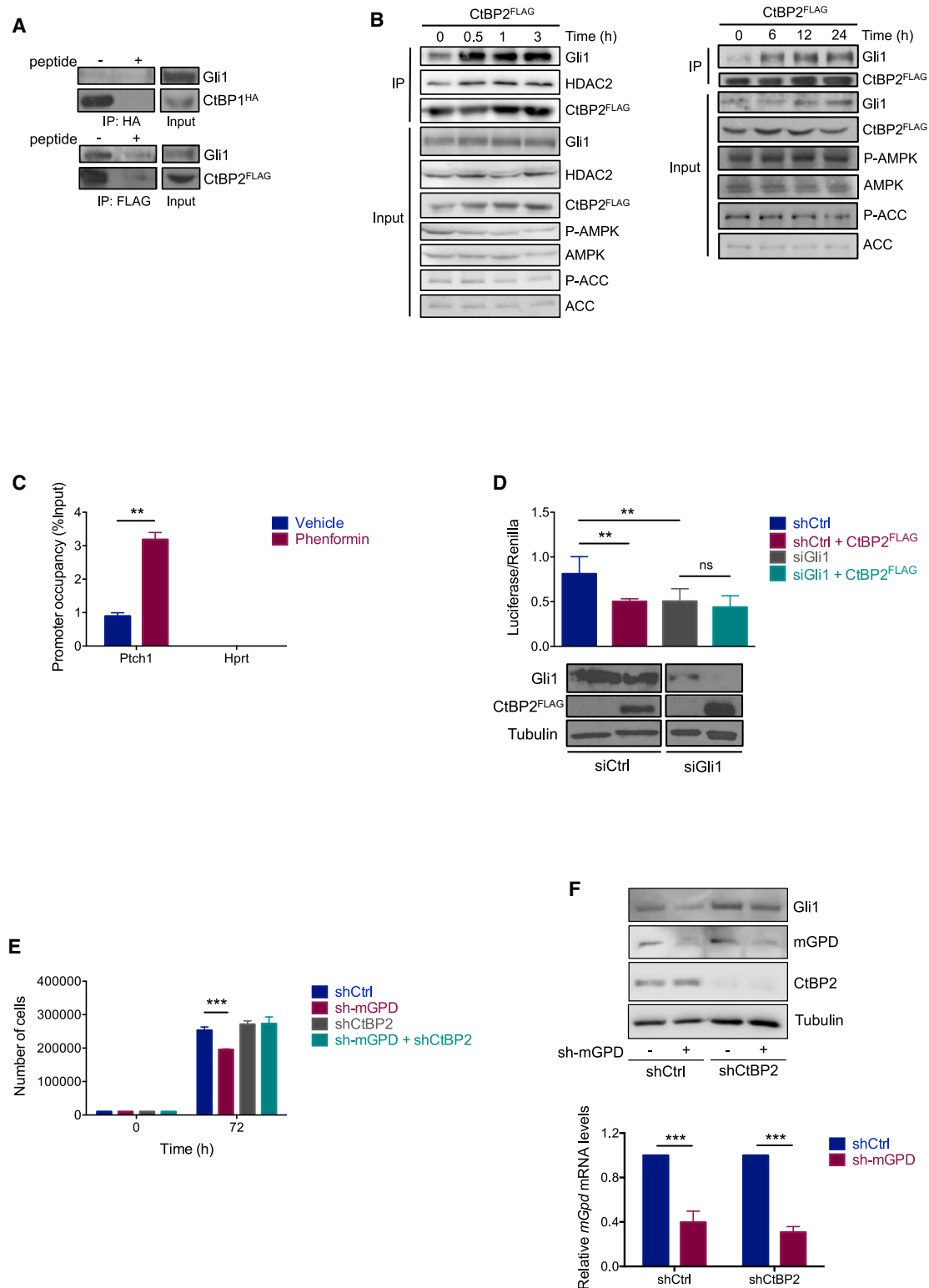
Figure 5. CtBP2 Acts as a Downstream Phenformin Mediator and Inhibits Gli1

(A) Immunoprecipitation assay on Med1-MB cells transiently transfected with hemagglutinin (HA)-tagged CtBP1 or FLAG-tagged CtBP2 plasmids. Lysates were immunoprecipitated with FLAG or HA antibodies, and western blot analysis was performed. Coimmunoprecipitated endogenous Gli1 protein levels are shown. Antibodies saturated with FLAG peptide and HA peptide before immunoprecipitation (IP) were used as negative controls.

(legend continued on next page)

by CtBP2 knockdown, clearly demonstrating the requirement of the redox sensor CtBP2 for the antitumor effect of mGPD.

To evaluate the pathophysiological relevance of this mechanism, we studied the phenformin response in CtBP2-deficient tumors. We transduced Med1-MB cells with lentiviruses expressing shCtBP2 or shControl shRNAs and tested their response to the biguanide. As shown in Figures S5B–S5D, phenformin failed to suppress tumor cell growth and Gli1 expression in cultured cells lacking CtBP2. We then grafted CtBP2-deficient or control Shh MB cells into immunodeficient nude mice until the tumor volumes reached 100 mm^3. Mice were divided in two groups (Figure S6A): one was treated with 300 mg/kg/day *per os,* and the other group was left untreated. The growth rate, tumor volumes, and weights were significantly reduced by phenformin in control Shh MB but were not affected by the drug in CtBP2-deficient tumors (Figures 6A and 6B). Supporting these results, Gli1 and Ki-67 levels (Figures 6C and 6D) were reduced by phenformin in control tumors but were unchanged in samples lacking CtBP2.

We also ruled out the involvement of mTOR signaling, as demonstrated by the unmodified p4E-BP1 and pS6 in CtBP2-deficient tumors from mice treated with phenformin at early and late time points (Figures 6C and 6E). Furthermore, CtBP2 levels were not modified by phenformin treatment (Figure S6B).

Altogether, these data demonstrate that the Gli1-CtBP2 complex formation, induced by mGPD-mediated increase of NADH, is a key event underlying the inhibitory effect of phenformin on Hh signaling and tumor growth (Figure 6F).

DISCUSSION

In this work, we have demonstrated that tumors characterized by inappropriate activation of the Hh pathway are markedly vulnerable to phenformin. A critical and controversial aspect for understanding the mechanism underlying growth inhibitory effects of phenformin has been selection of a dosage range that accurately reflects dosage used in therapeutic settings. Based on previous observations in patients, observations in mice and our own analyses, we have established that 1–5 μM is the appropriate concentration range to achieve therapeutic benefit of phenformin. Circulating levels beyond these values were not tolerated in our animal models and, to our knowledge, have never been reported in patients. Another important parameter that we have carefully evaluated is the glucose concentration, which was maintained within the physiological range. In this regard, a previous work (Birsoy et al., 2014) showed that glucose utilization defects or impaired respiration are important determinants for tumor cell sensitivity to biguanides and glucose limitations (Birsoy et al., 2014). Consistent with those observations, we found that Shh MB tumor cells are more sensitive to phenformin under low glucose conditions and show markers of glucose utilization defects, but not of impaired respiration.

In some tumors, the therapeutic properties of biguanides have been attributed to their ability to lower insulin/insulin growth factor 1 (IGF1) signaling (Algire et al., 2011; Goodwin et al., 2008) through a systemic, indirect effect. However, this mechanism appears to be of particular relevance to hyperinsulinemic tumor patients, whose cancer may be growth-stimulated by insulin (Algire et al., 2011; Pollak, 2012). We ruled out contribution of the insulin/IGF1 pathway in our studies by using normoglycemic animals and by ascertaining that insulin signaling was not altered in Shh MB tumors from phenformin-treated mice (data not shown).

In this study, we have also demonstrated that the antitumor effect of phenformin on Shh MB is independent of respiratory complex I and the associated perturbations of the energy balance. Complex I has been a topic of extensive debate and was demonstrated to be an important mechanism for biguanide action in several studies (Fontaine, 2018; He and Wondisford, 2015; Rena et al., 2017). A major concern is that although the concentrations of biguanides to inhibit purified complex I in cell-free biochemical assays are within the supra-physiological millimolar range (Bridges et al., 2014; Owen et al., 2000; Wheaton et al., 2014), the mean plasma and tissue levels of the drugs are hundreds of times lower, even after administration of the maximum tolerated doses (Nattrass et al., 1980; Scheen, 1996). Studies have proposed a plausible explanation for this apparent discrepancy. It has been observed that due to their positive charge, biguanides tend to accumulate in the mitochondrial matrix in a voltage-dependent manner (Bridges et al., 2014). In particular, it was shown that phenformin accumulates in the mitochondria and reaches the maximum levels within 6 h, with a half maximal inhibitory concentration (IC$_{50}$) for complex I inhibition within the micromolar range (Bridges et al., 2014).

Recently, using a methodology called 4-[^{18}F]fluorobenzyl-triphenylphosphonium (^{18}F-BnTP PET) imaging, which allows detection of *in vivo* changes of mitochondrial membrane potential, Momcilovic and colleagues showed that in lung cancer cells, administration of phenformin decreases the uptake of the tracer,

---

(B) Med1-MB cells were transfected with FLAG-tagged CtBP2 and treated with phenformin (5 μM) for the indicated times. Cellular extracts were immunoprecipitated with FLAG antibody and analyzed by western blot. Endogenous Gli1 protein levels are shown.

(C) Chromatin immunoprecipitation (ChIP) assay on Med1-MB cells treated with vehicle (DMEM) or phenformin (5 μM) for 6 h. Immunoprecipitation was performed with a CtBP2-specific antibody, and fold enrichment over immunoglobulin G (IgG) control was determined by qPCR analysis with primers encompassing the *Ptch1* promoter. *Hprt* was used as negative control.

(D) Effects of CtBP2 overexpression on Gli1 transcriptional activity in Med1-MB cells expressing siControl (siCtrl) or Gli1-specific siRNA, evaluated as luciferase to Renilla ratios. Non-contiguous lanes are indicated.

(E) Cell proliferation assay in Med1-MB cells stably transduced with lentiviruses expressing control (shCtrl), mGPD, and CtBP2-specific shRNAs alone or in combination for 72 h.

(F) Top: Gli1, CtBP2, and mGPD protein levels from Med1-MB cells transduced as above were analyzed by western blot. Bottom: *mGPD* mRNA levels were analyzed by qPCR.

All data are represented as the mean ± SD of three independent experiments, each performed in triplicate. **p < 0.01, ***p < 0.001, ns, not significant, by ANOVA and unpaired t test.

See also Figure S5 and Table S1.

A

B

C

D

E

F
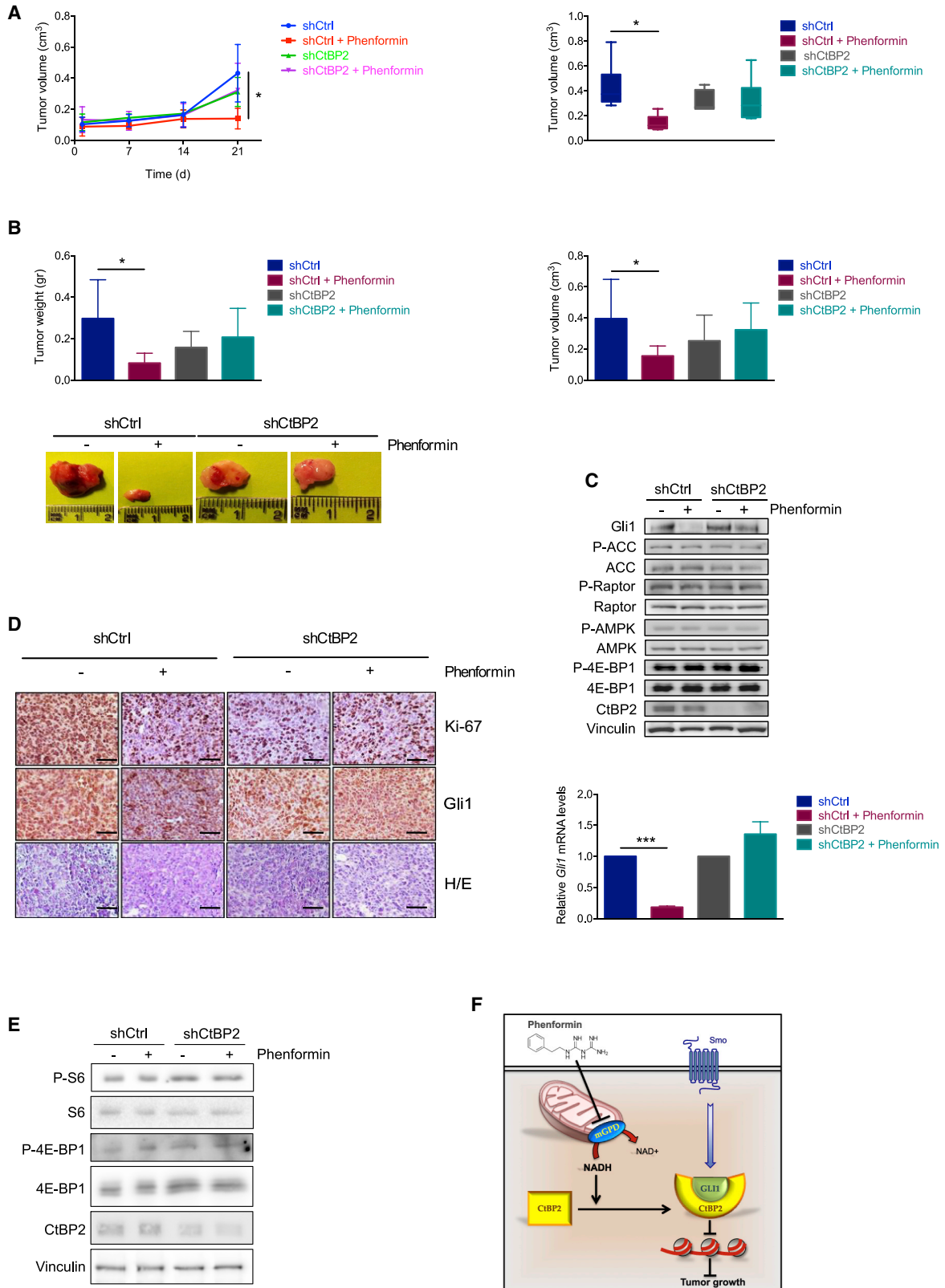
(legend on next page)

indicating the ability of the biguanide to lower membrane potential ($\Delta\Psi$), a consequence attributed by the authors to complex I inhibition (Momcilovic et al., 2019).

In contrast with these studies, we found that when given at therapeutic doses (i.e., 5 μM), phenformin did not affect complex I activity, as assessed by several parameters. Despite the use of multiple time and dose-dependent regimens, OCR, ATP levels, and TCA cycle metabolites remained unmodified, and AMPK, mTOR, and adenylyl cyclase activities were unchanged. More importantly, phenformin continued to inhibit tumor growth and Hh signaling even after inactivation of complex I and its substitution with the rotenone-insensitive NDI1.

Previous observations showed that expression of NDI1 abrogated the inhibitory effect of phenformin on tumor growth in grafted cancer cell lines (Birsoy et al., 2014). However, the cells used in that work carried mutations of mitochondrial complex I, and NDI1 expression was used to rescue this primary defect. Conversely, because mitochondrial function is intact in our Shh MB cells, while glucose utilization is impaired, NDI1 expression is not expected to rescue cell growth or Gli1 levels after phenformin treatment.

In keeping with our results, previous studies found that when compared with control patients, TCA cycle metabolites and pAMPK are not modified in tumor samples from biguanide-treated breast cancer patients (Lord et al., 2018). Moreover, a recent report showed that administration of therapeutic doses of metformin induced an increase of cellular respiration in liver, arguing against complex I inhibition as the main mechanism of action of biguanides, at least in that context (Wang et al., 2019).

The difference between the observations on complex I inhibition can be due to various reasons. First, emerging studies are showing that tumor cells display different permeability and retention capacity for biguanides, resulting in various degrees of accumulation of the drug in the mitochondria (Iversen et al., 2017). In addition, the route of administration may lead to different tissue distributions and concentrations of the drug. Hence, the intracellular concentration reached in the various districts may depend on local permeability and conditions used. In addition, the concentration of nutrients in cell culture such as glucose or pyruvate may influence the effect of the biguanides (Birsoy et al., 2014) by changing the activity of mitochondria and thus the potential difference and the degree of biguanide accumulation. Finally, even if the calculated low-micromolar IC$_{50}$ of phenformin is close to the C$_{max}$ value observed after administration of the maximum tolerated dose, this concentration is not maintained for the subsequent hours and instead declines

quickly (Figures 1B and 1C). Pharmacokinetics studies show that biguanides enter but do not accumulate in large amounts in tissues (Gormsen et al., 2016; Graham et al., 2011). Thus, it is possible that under physiological conditions, the average circulating concentration may be insufficient for mitochondrial accumulation and complex I inhibition in certain tumors.

Although the energy balance seems to be unaffected, we have shown that the key event underlying the effect of phenformin in Shh MB is the mGPD-mediated increase of the redox state, leading to an elevation of NADH levels. These results support the findings by Madiraju et al. (2014, 2018), who showed that at therapeutic doses, biguanides inhibit the glycerophosphate shuttle in the liver, resulting in an accumulation of lactate and inhibition of hepatic gluconeogenesis without changing in the energy balance or OCR. Biguanides inhibit mGPD activity *in vitro* with an approximate inhibition constant (Ki) value close to the therapeutic range of circulating levels observed in patients and animal models (Hulea et al., 2018; Madiraju et al., 2014).

mGPD catalyzes the oxidation of G3P to dihydroxyacetone phosphate (DHAP) and the parallel reduction of FAD+ to FADH$_2$. DHAP is in turn reduced to G3P at the expense of NADH oxidation to NAD+ by the cytosolic cGPD enzyme. Both cGPD and mGPD are part of a coupled mechanism responsible for transferring reducing equivalents from the cytosol to the mitochondria, because the mitochondrial membrane is impermeable to NADH. Thus, inhibition of mGPD results in alterations of the mitochondrial membrane voltage $\Delta\Psi$ (Orr et al., 2014).

The function of the hepatic GPD shuttle appears of particular relevance when the body relies mostly on triglycerides (TG) to maintain normal blood glucose levels. Conditions like fasting, insulin resistance, and diabetes are characterized by increased TG release from adipose tissue, which are in turn de-esterified in the liver to release G3P. G3P is then oxidized into DHAP, a key intermediate of gluconeogenesis. Thus, the availability of G3P from TG represents a key determinant for GPD-mediated hepatic gluconeogenesis, and this process is inhibited by biguanides with consequent accumulation of lactate and cytoplasmic NADH (Petersen et al., 2017).

Our observations indicate that inhibition of mGPD in tumor cells leads to the same alterations observed in hepatocytes, suggesting that Shh MB cells may also have elevated levels of G3P available for oxidation. In this regard, a previous report showed elevated content of TG in Shh MB cells as a consequence of an E2F1-mediated induction of FASN (Bhatia et al., 2011).

Figure 6. CtBP2-Deficient Tumors Are Insensitive to Phenformin

(A) Med1-MB cells were transduced with a lentivirus expressing shCtrl or shCtBP2 and injected into the flanks of NOD/SCID mice, which were randomly divided and treated with vehicle (water) or phenformin (300 mg/kg/day) in the drinking water. (Left) Measurements of tumor volumes over time. n = 5. (Right) Boxplots representing the mean tumor burden following 4 weeks of treatment.

(B) Tumor weight (left) and volume (right) at the end of the treatment. (Bottom) Images of excised flank allografts from the treatment groups.

(C) Lysates from the tumor allografts described above were immunoblotted with the indicated antibodies (top), and *Gli1* mRNA levels were analyzed by qPCR (bottom).

(D) Immunohistochemical analysis of representative allograft tumors from above stained with the indicated antibodies or H&E. Scale bar, 70 μm.

(E) Med1-MB cells stably expressing shCtrl or shCtBP2 were injected into the flanks of NOD/SCID mice, which were i.v. treated with vehicle (water) or phenformin (12.5 mg/kg) for 2 h. Tumor lysates were immunoblotted with the indicated antibodies. n = 5.

(F) Model of the mGPD-CtBP2-mediated phenformin effect on tumor growth. Phenformin treatment inhibits mGPD, causing an increase of cellular NADH. The altered redox state promotes an association between CtBP2 and Gli1, inhibiting Hh target gene expression and tumor growth.

All data are represented as the mean ± SD of three independent experiments, each performed in triplicate. *p < 0.05, ***p < 0.001, as determined by ANOVA test. See also Figure S6 and Tables S1 and S2.

Such an observation would be consistent with an increased availability of G3P and an increased mGPD-mediated oxidation to DHAP, a process inhibited by phenformin with consequent NADH accumulation. Because DHAP is also generated from glucose metabolism and an accumulation of DHAP would reduce G3P oxidation, this metabolic scenario supports the observation that phenformin displays higher efficacy when glucose concentrations are low and glucose metabolism is impaired, evidence also reported by other authors (Birsoy et al., 2014). To reconcile our findings with previous observations, it could be hypothesized that cells with defects in mitochondrial function or glucose utilization may engage alternative compensatory mechanisms, such as the glycerophosphate shuttle, for their energy demand and thus become sensitive to phenformin-mediated inhibition of mGPD. Experiments to carefully distinguish between the role of complex I versus the mGPD inhibition in different contexts will be required to clarify this issue.

A central finding of this report is that the antitumor effect of phenformin is linked to the elevation of the redox state, not to inhibition of respiration and energy balance. A key player of this mechanism is the CtBP2 corepressor, which responds to the raise in NADH increasing the binding with Gli1, leading to inhibition of Hh target genes.

CtBP1 and CtBP2 are conserved corepressors involved in developmental processes that act as redox sensors through their NADH-binding domain (Chinnadurai, 2002). Upon binding to NADH, CtBPs undergo a conformational change that promotes association with binding partners through a conserved PXDLS motif present in several transcriptional factors (Kumar et al., 2002; Zhang et al., 2000, 2002). CtBPs interact with transcriptional repressors like HDAC1/2 and LSD1 through other (non-PXDLS) binding regions (Blevins et al., 2017). Gli1 does not have a conserved PXDLS motif, suggesting that it interacts with CtBP2 via other interaction domains. Alternately, CtBP2 may associate with Gli1 indirectly within a protein complex with HDAC1/2, previously reported to interact with Gli1 (Canettieri et al., 2010). In agreement with this latter hypothesis, the association of CtBP2 with HDAC2 is enhanced by phenformin.

CtBPs seem to play a context-dependent role in cancer by either supporting or inhibiting tumorigenesis. Indeed, in some tumors, such as prostate cancer and melanoma, CtBPs have been described as a tumor suppressors, whereas in several other tumors, CtBPs are upregulated and positively associated with pro-tumorigenic functions (Blevins et al., 2017).

In our study, CtBP2 acts as a tumor suppressor by associating with Gli1 and limiting its transcriptional activity in Shh MB cells. CtBP2-Gli1 association and transcriptional repression is promoted by phenformin at therapeutic doses that alter the redox state unrelated to energy status of the cell.

The function of CtBP as a redox sensor has mostly been examined using drugs or conditions like hypoxia or 2-deoxyglucose (2DG), which affect both redox and energy states (Shen et al., 2017; Zhang et al., 2006). In this study, phenformin treatment or mGPD knockdown perturbs only the redox state, suggesting a need for additional examination of such a decoupling of CtBP activation from metabolism-driven mechanisms that also have a profound impact on cancer cells.

An important question that arises from this study is the applicability of this mechanism to other cancers. Tumors sustained by the same molecular pathology, i.e., elevated Hh/Gli1 signaling, appear to operate by the same mechanism that we have elucidated in this study. It is likely that in addition to Hh-driven tumors, CtBPs might exert their antitumor effects in other phenformin-sensitive tumors by associating with proteins that affect tumorigenesis upon redox-induced conformational change. A study of the CtBP-binding partners under conditions of increased redox state will help to clarify this interesting aspect.

Finally, our data show the significant preclinical efficacy of phenformin on Shh MB through inhibition of Gli1. Of note, the ability of phenformin to suppress Hh signaling in SuFu-deficient MB cells suggests that this drug could potentially be a weapon against Hh-dependent tumors resistant to Smo inhibitors.

Phenformin has shown stronger anticancer properties compared with metformin in most tumors studied, likely due to higher hydrophobicity and permeability (Janzer et al., 2014). This is also believed to be the reason of the higher risk of lactic acidosis, a primary concern associated with the use of this drug. However, the remarkable inhibitory effect observed in different types of cancers in preclinical settings has generated renewed interest in using phenformin for treatment of other cancer patients. In this regard, it will be important to carefully establish the toxicity and tolerability of phenformin at various doses and times in cancer patients. Although no trials are still being carried out in patients with brain tumors, a phase Ib clinical trial using a combination of phenformin with BRAF inhibitors in patients with metastatic melanoma is under way (Clincaltrials.gov identifier NCT03026517). Results from this trial will provide useful preliminary clinical information about the use of phenformin in cancer patients.

In summary, we have identified a mechanism whereby the direct antitumor effects of phenformin at the therapeutic plasma concentrations depend on the inhibition of the glycerophosphate shuttle, with consequent increase of the redox state. By contrast, our data rule out the involvement of complex I and of the energy-sensing machinery (i.e., AMPK and mTOR signaling) in the tumor-inhibitory effect of phenformin. Based on our work and previous observations, we propose that there could be more than one antitumor mechanism for phenformin that operates *in vivo*, depending on context.

STAR★METHODS

Detailed methods are provided in the online version of this paper and include the following:

- KEY RESOURCES TABLE
- LEAD CONTACT AND MATERIALS AVAILABILITY
- EXPERIMENTAL MODEL AND SUBJECT DETAILS
  - Cell lines and cultures
  - *In vivo* mouse studies
- METHOD DETAILS
  - Transfections and luciferase assays
  - Determination of cell proliferation and tumorspheres size

- ○ Western blotting, immunoprecipitation and phosphorylation assays
- ○ Plasmids and antibodies
- ○ Lentiviral-mediated shRNA knockdown and retroviral delivery
- ○ Quantitative Real-Time PCR (qPCR) assay
- ○ Chromatin immunoprecipitation (ChIP) assay
- ○ Immunohistochemistry (IHC)
- ○ Determination of phenformin concentration
- ○ Metabolic assays
- ○ Analysis of metabolites by GC-MS
- ○ mGPD activity assay
- ○ NMR metabolomics
- ● QUANTIFICATION AND STATISTICAL ANALYSIS
- ● DATA AND CODE AVAILABILITY

SUPPLEMENTAL INFORMATION

Supplemental Information can be found online at https://doi.org/10.1016/j.celrep.2020.01.024.

AUTHOR CONTRIBUTIONS

L. Di Magno designed and performed experiments, analyzed data with assistance from S.M. and F.D.P., and wrote the paper; S. Coni, A.M., S. Cairoli, M.S., P.I., M. Moretti, M.P., C.N., and E.I. performed experiments; C.C., E.D.S., L. Di Marcotullio, G.G., L.B., B.M.G., E.A., and M. Maroder analyzed data and critically read the manuscript; and G.C. conceived the study, designed experiments, analyzed data, and wrote the paper.

DECLARATION OF INTERESTS

The authors declare no competing interests.

REFERENCES

Algire, C., Amrein, L., Bazile, M., David, S., Zakikhani, M., and Pollak, M. (2011). Diet and tumor LKB1 expression interact to determine sensitivity to anti-neoplastic effects of metformin in vivo. Oncogene 30, 1174–1182.

Antonucci, L., D'Amico, D., Di Magno, L., Coni, S., Di Marcotullio, L., Cardinali, B., Gulino, A., Ciapponi, L., and Canettieri, G. (2014). CNBP regulates wing development in Drosophila melanogaster by promoting IRES-dependent translation of dMyc. Cell Cycle 13, 434–439.

Appleyard, M.V., Murray, K.E., Coates, P.J., Wullschleger, S., Bray, S.E., Kernohan, N.M., Fleming, S., Alessi, D.R., and Thompson, A.M. (2012). Phenformin as prophylaxis and therapy in breast cancer xenografts. Br. J. Cancer 106, 1117–1122.

Aszterbaum, M., Epstein, J., Oro, A., Douglas, V., LeBoit, P.E., Scott, M.P., and Epstein, E.H., Jr. (1999). Ultraviolet and ionizing radiation enhance the growth of BCCs and trichoblastomas in patched heterozygous knockout mice. Nat. Med. 5, 1285–1291.

Bando, K., Ochiai, S., Kunimatsu, T., Deguchi, J., Kimura, J., Funabashi, H., and Seki, T. (2010). Comparison of potential risks of lactic acidosis induction by biguanides in rats. Regul. Toxicol. Pharmacol. 58, 155–160.

Barczak, W., Suchorska, W., Rubiś, B., and Kulcenty, K. (2015). Universal real-time PCR-based assay for lentiviral titration. Mol. Biotechnol. 57, 195–200.

Beauchamp, E., Bulut, G., Abaan, O., Chen, K., Merchant, A., Matsui, W., Endo, Y., Rubin, J.S., Toretsky, J., and Uren, A. (2009). GLI1 is a direct transcriptional target of EWS-FLI1 oncoprotein. J. Biol. Chem. 284, 9074–9082.

Beauchamp, E.M., Ringer, L., Bulut, G., Sajwan, K.P., Hall, M.D., Lee, Y.C., Peaceman, D., Ozdemirli, M., Rodriguez, O., Macdonald, T.J., et al. (2011). Arsenic trioxide inhibits human cancer cell growth and tumor development in mice by blocking Hedgehog/GLI pathway. J. Clin. Invest. 121, 148–160.

Berger, W. (1985). Incidence of severe sideeffects during therapy with sulfonylureas and biguanides. Horm. Metab. Res. Suppl. 15, 111–115.

Bhatia, B., Hsieh, M., Kenney, A.M., and Nahlé, Z. (2011). Mitogenic Sonic hedgehog signaling drives E2F1-dependent lipogenesis in progenitor cells and medulloblastoma. Oncogene 30, 410–422.

Birsoy, K., Possemato, R., Lorbeer, F.K., Bayraktar, E.C., Thiru, P., Yucel, B., Wang, T., Chen, W.W., Clish, C.B., and Sabatini, D.M. (2014). Metabolic determinants of cancer cell sensitivity to glucose limitation and biguanides. Nature 508, 108–112.

Birsoy, K., Wang, T., Chen, W.W., Freinkman, E., Abu-Remaileh, M., and Sabatini, D.M. (2015). An Essential Role of the Mitochondrial Electron Transport Chain in Cell Proliferation Is to Enable Aspartate Synthesis. Cell 162, 540–551.

Blevins, M.A., Huang, M., and Zhao, R. (2017). The Role of CtBP1 in Oncogenic Processes and Its Potential as a Therapeutic Target. Mol. Cancer Ther. 16, 981–990.

Bridges, H.R., Jones, A.J., Pollak, M.N., and Hirst, J. (2014). Effects of metformin and other biguanides on oxidative phosphorylation in mitochondria. Biochem. J. 462, 475–487.

Briscoe, J., and Thérond, P.P. (2013). The mechanisms of Hedgehog signalling and its roles in development and disease. Nat. Rev. Mol. Cell Biol. 14, 416–429.

Canese, R., Palombelli, G., Chirico, M., Sestili, P., Bagnoli, M., Canevari, S., Mezzanzanica, D., Podo, F., and Iorio, E. (2019). Integration of MRI and MRS approaches to monitor molecular imaging and metabolomic effects of trabectedin on a preclinical ovarian cancer model. NMR Biomed. 32, e4016.

Canettieri, G., Coni, S., Della Guardia, M., Nocerino, V., Antonucci, L., Di Magno, L., Screaton, R., Screpanti, I., Giannini, G., and Gulino, A. (2009). The coactivator CRTC1 promotes cell proliferation and transformation via AP-1. Proc. Natl. Acad. Sci. USA 106, 1445–1450.

Canettieri, G., Di Marcotullio, L., Greco, A., Coni, S., Antonucci, L., Infante, P., Pietrosanti, L., De Smaele, E., Ferretti, E., Miele, E., et al. (2010). Histone deacetylase and Cullin3-REN(KCTD11) ubiquitin ligase interplay regulates Hedgehog signalling through Gli acetylation. Nat. Cell Biol. 12, 132–142.

Cardaci, S., Zheng, L., MacKay, G., van den Broek, N.J., MacKenzie, E.D., Nixon, C., Stevenson, D., Tumanov, S., Bulusu, V., Kamphorst, J.J., et al. (2015). Pyruvate carboxylation enables growth of SDH-deficient cells by supporting aspartate biosynthesis. Nat. Cell Biol. 17, 1317–1326.

Che, J., Zhang, F.Z., Zhao, C.Q., Hu, X.D., and Fan, S.J. (2013). Cyclopamine is a novel Hedgehog signaling inhibitor with significant anti-proliferative, anti-invasive and anti-estrogenic potency in human breast cancer cells. Oncol. Lett. 5, 1417–1421.

Cheng, C.L., and Chou, C.H. (2001). Determination of metformin in human plasma by high-performance liquid chromatography with spectrophotometric detection. J. Chromatogr. B Biomed. Sci. Appl. 762, 51–58.

Chida, J., Yamane, K., Takei, T., and Kido, H. (2012). An efficient extraction method for quantitation of adenosine triphosphate in mammalian tissues and cells. Anal. Chim. Acta 727, 8–12.

Chinnadurai, G. (2002). CtBP, an unconventional transcriptional corepressor in development and oncogenesis. Mol. Cell *9*, 213–224.

Coni, S., Antonucci, L., D'Amico, D., Di Magno, L., Infante, P., De Smaele, E., Giannini, G., Di Marcotullio, L., Screpanti, I., Gulino, A., and Canettieri, G. (2013). Gli2 acetylation at lysine 757 regulates hedgehog-dependent transcriptional output by preventing its promoter occupancy. PLoS ONE *8*, e65718.

Coni, S., Mancuso, A.B., Di Magno, L., Sdruscia, G., Manni, S., Serrao, S.M., Rotili, D., Spiombi, E., Bufalieri, F., Petroni, M., et al. (2017). Selective targeting of HDAC1/2 elicits anticancer effects through Gli1 acetylation in preclinical models of SHH Medulloblastoma. Sci. Rep. *7*, 44079.

D'Amico, D., Antonucci, L., Di Magno, L., Coni, S., Sdruscia, G., Macone, A., Miele, E., Infante, P., Di Marcotullio, L., De Smaele, E., et al. (2015). Non-canonical Hedgehog/AMPK-Mediated Control of Polyamine Metabolism Supports Neuronal and Medulloblastoma Cell Growth. Dev. Cell *35*, 21–35.

Di Magno, L., Manzi, D., D'Amico, D., Coni, S., Macone, A., Infante, P., Di Marcotullio, L., De Smaele, E., Ferretti, E., Screpanti, I., et al. (2014). Druggable glycolytic requirement for Hedgehog-dependent neuronal and medulloblastoma growth. Cell Cycle *13*, 3404–3413.

Di Magno, L., Coni, S., Di Marcotullio, L., and Canettieri, G. (2015). Digging a hole under Hedgehog: downstream inhibition as an emerging anticancer strategy. Biochim. Biophys. Acta *1856*, 62–72.

Di Magno, L., Basile, A., Coni, S., Manni, S., Sdruscia, G., D'Amico, D., Antonucci, L., Infante, P., De Smaele, E., Cucchi, D., et al. (2016). The energy sensor AMPK regulates Hedgehog signaling in human cells through a unique Gli1 metabolic checkpoint. Oncotarget *7*, 9538–9549.

Dykens, J.A., Jamieson, J., Marroquin, L., Nadanaciva, S., Billis, P.A., and Will, Y. (2008). Biguanide-induced mitochondrial dysfunction yields increased lactate production and cytotoxicity of aerobically-poised HepG2 cells and human hepatocytes *in vitro*. Toxicol. Appl. Pharmacol. *233*, 203–210.

El-Mir, M.Y., Nogueira, V., Fontaine, E., Avéret, N., Rigoulet, M., and Leverve, X. (2000). Dimethylbiguanide inhibits cell respiration via an indirect effect targeted on the respiratory chain complex I. J. Biol. Chem. *275*, 223–228.

Fontaine, E. (2018). Metformin-Induced Mitochondrial Complex I Inhibition: Facts, Uncertainties, and Consequences. Front. Endocrinol. (Lausanne) *9*, 753.

Foretz, M., Hébrard, S., Leclerc, J., Zarrinpashneh, E., Soty, M., Mithieux, G., Sakamoto, K., Andreelli, F., and Viollet, B. (2010). Metformin inhibits hepatic gluconeogenesis in mice independently of the LKB1/AMPK pathway via a decrease in hepatic energy state. J. Clin. Invest. *120*, 2355–2369.

Foretz, M., Guigas, B., Bertrand, L., Pollak, M., and Viollet, B. (2014). Metformin: from mechanisms of action to therapies. Cell Metab. *20*, 953–966.

Glunde, K., Raman, V., Mori, N., and Bhujwalla, Z.M. (2005). RNA interference-mediated choline kinase suppression in breast cancer cells induces differentiation and reduces proliferation. Cancer Res. *65*, 11034–11043.

Goodrich, L.V., Milenković, L., Higgins, K.M., and Scott, M.P. (1997). Altered neural cell fates and medulloblastoma in mouse patched mutants. Science *277*, 1109–1113.

Goodwin, P.J., Pritchard, K.I., Ennis, M., Clemons, M., Graham, M., and Fantus, I.G. (2008). Insulin-lowering effects of metformin in women with early breast cancer. Clin. Breast Cancer *8*, 501–505.

Gormsen, L.C., Sundelin, E.I., Jensen, J.B., Vendelbo, M.H., Jakobsen, S., Munk, O.L., Hougaard Christensen, M.M., Brøsen, K., Frøkiær, J., and Jessen, N. (2016). In Vivo Imaging of Human 11C-Metformin in Peripheral Organs: Dosimetry, Biodistribution, and Kinetic Analyses. J. Nucl. Med. *57*, 1920–1926.

Götschel, F., Berg, D., Gruber, W., Bender, C., Eberl, M., Friedel, M., Sonntag, J., Rüngeler, E., Hache, H., Wierling, C., et al. (2013). Synergism between Hedgehog-GLI and EGFR signaling in Hedgehog-responsive human medulloblastoma cells induces downregulation of canonical Hedgehog-target genes and stabilized expression of GLI1. PLoS ONE *8*, e65403.

Graham, G.G., Punt, J., Arora, M., Day, R.O., Doogue, M.P., Duong, J.K., Furlong, T.J., Greenfield, J.R., Greenup, L.C., Kirkpatrick, C.M., et al. (2011). Clinical pharmacokinetics of metformin. Clin. Pharmacokinet. *50*, 81–98.

Gruber, W., Peer, E., Elmer, D.P., Sternberg, C., Tesanovic, S., Del Burgo, P., Coni, S., Canettieri, G., Neureiter, D., Bartz, R., et al. (2018). Targeting class I histone deacetylases by the novel small molecule inhibitor 4SC-202 blocks oncogenic hedgehog-GLI signaling and overcomes smoothened inhibitor resistance. Int. J. Cancer *142*, 968–975.

Hayden Gephart, M.G., Su, Y.S., Bandara, S., Tsai, F.C., Hong, J., Conley, N., Rayburn, H., Milenkovic, L., Meyer, T., and Scott, M.P. (2013). Neuropilin-2 contributes to tumorigenicity in a mouse model of Hedgehog pathway medulloblastoma. J. Neurooncol. *115*, 161–168.

He, L., and Wondisford, F.E. (2015). Metformin action: concentrations matter. Cell Metab. *21*, 159–162.

Huang, X., Wullschleger, S., Shpiro, N., McGuire, V.A., Sakamoto, K., Woods, Y.L., McBurnie, W., Fleming, S., and Alessi, D.R. (2008). Important role of the LKB1-AMPK pathway in suppressing tumorigenesis in PTEN-deficient mice. Biochem. J. *412*, 211–221.

Hulea, L., Gravel, S.P., Morita, M., Cargnello, M., Uchenunu, O., Im, Y.K., Lehuédé, C., Ma, E.H., Leibovitch, M., McLaughlan, S., et al. (2018). Translational and HIF-1α-Dependent Metabolic Reprogramming Underpin Metabolic Plasticity and Responses to Kinase Inhibitors and Biguanides. Cell Metab. *28*, 817–832.

Infante, P., Mori, M., Alfonsi, R., Ghirga, F., Aiello, F., Toscano, S., Ingallina, C., Siler, M., Cucchi, D., Po, A., et al. (2015). Gli1/DNA interaction is a druggable target for Hedgehog-dependent tumors. EMBO J. *34*, 200–217.

Iorio, E., Ricci, A., Bagnoli, M., Pisanu, M.E., Castellano, G., Di Vito, M., Venturini, E., Glunde, K., Bhujwalla, Z.M., Mezzanzanica, D., et al. (2010). Activation of phosphatidylcholine cycle enzymes in human epithelial ovarian cancer cells. Cancer Res. *70*, 2126–2135.

Iversen, A.B., Horsman, M.R., Jakobsen, S., Jensen, J.B., Garm, C., Jessen, N., Breining, P., Frøkiær, J., and Busk, M. (2017). Results from 11C-metformin-PET scans, tissue analysis and cellular drug-sensitivity assays questions the view that biguanides affects tumor respiration directly. Sci. Rep. *7*, 9436.

Jackson, A.L., Sun, W., Kilgore, J., Guo, H., Fang, Z., Yin, Y., Jones, H.M., Gilliam, T.P., Zhou, C., and Bae-Jump, V.L. (2017). Phenformin has anti-tumorigenic effects in human ovarian cancer cells and in an orthotopic mouse model of serous ovarian cancer. Oncotarget *8*, 100113–100127.

Janzer, A., German, N.J., Gonzalez-Herrera, K.N., Asara, J.M., Haigis, M.C., and Struhl, K. (2014). Metformin and phenformin deplete tricarboxylic acid cycle and glycolytic intermediates during cell transformation and NTPs in cancer stem cells. Proc. Natl. Acad. Sci. USA *111*, 10574–10579.

Kalender, A., Selvaraj, A., Kim, S.Y., Gulati, P., Brûlé, S., Viollet, B., Kemp, B.E., Bardeesy, N., Dennis, P., Schlager, J.J., et al. (2010). Metformin, independent of AMPK, inhibits mTORC1 in a rag GTPase-dependent manner. Cell Metab. *11*, 390–401.

Kenney, A.M., and Rowitch, D.H. (2000). Sonic hedgehog promotes G(1) cyclin expression and sustained cell cycle progression in mammalian neuronal precursors. Mol. Cell. Biol. *20*, 9055–9067.

Kim, J., Aftab, B.T., Tang, J.Y., Kim, D., Lee, A.H., Rezaee, M., Kim, J., Chen, B., King, E.M., Borodovsky, A., et al. (2013). Itraconazole and arsenic trioxide inhibit Hedgehog pathway activation and tumor growth associated with acquired resistance to smoothened antagonists. Cancer Cell *23*, 23–34.

Kumar, V., Carlson, J.E., Ohgi, K.A., Edwards, T.A., Rose, D.W., Escalante, C.R., Rosenfeld, M.G., and Aggarwal, A.K. (2002). Transcription corepressor CtBP is an NAD(+)-regulated dehydrogenase. Mol. Cell *10*, 857–869.

Li, Y.H., Luo, J., Mosley, Y.Y., Hedrick, V.E., Paul, L.N., Chang, J., Zhang, G., Wang, Y.K., Banko, M.R., Brunet, A., et al. (2015). AMP-Activated Protein Kinase Directly Phosphorylates and Destabilizes Hedgehog Pathway Transcription Factor GLI1 in Medulloblastoma. Cell Rep. *12*, 599–609.

Lord, S.R., Cheng, W.C., Liu, D., Gaude, E., Haider, S., Metcalf, T., Patel, N., Teoh, E.J., Gleeson, F., Bradley, K., et al. (2018). Integrated Pharmacodynamic Analysis Identifies Two Metabolic Adaption Pathways to Metformin in Breast Cancer. Cell Metab. *28*, 679–688.

Madiraju, A.K., Erion, D.M., Rahimi, Y., Zhang, X.M., Braddock, D.T., Albright, R.A., Prigaro, B.J., Wood, J.L., Bhanot, S., MacDonald, M.J., et al. (2014).

Metformin suppresses gluconeogenesis by inhibiting mitochondrial glycerophosphate dehydrogenase. Nature 510, 542–546.

Madiraju, A.K., Qiu, Y., Perry, R.J., Rahimi, Y., Zhang, X.M., Zhang, D., Camporez, J.G., Cline, G.W., Butrico, G.M., Kemp, B.E., et al. (2018). Metformin inhibits gluconeogenesis via a redox-dependent mechanism in vivo. Nat. Med. 24, 1384–1394.

Miller, R.A., Chu, Q., Xie, J., Foretz, M., Viollet, B., and Birnbaum, M.J. (2013). Biguanides suppress hepatic glucagon signalling by decreasing production of cyclic AMP. Nature 494, 256–260.

Momcilovic, M., Jones, A., Bailey, S.T., Waldmann, C.M., Li, R., Lee, J.T., Abdelhady, G., Gomez, A., Holloway, T., Schmid, E., et al. (2019). In vivo imaging of mitochondrial membrane potential in non-small-cell lung cancer. Nature 575, 380–384.

Nattrass, M., Sizer, K., and Alberti, K.G. (1980). Correlation of plasma phenformin concentration with metabolic effects in normal subjects. Clin. Sci. (Lond.) 58, 153–155.

Orr, A.L., Ashok, D., Sarantos, M.R., Ng, R., Shi, T., Gerencser, A.A., Hughes, R.E., and Brand, M.D. (2014). Novel inhibitors of mitochondrial sn-glycerol 3-phosphate dehydrogenase. PLoS ONE 9, e89938.

Ota, S., Horigome, K., Ishii, T., Nakai, M., Hayashi, K., Kawamura, T., Kishino, A., Taiji, M., and Kimura, T. (2009). Metformin suppresses glucose-6-phosphatase expression by a complex I inhibition and AMPK activation-independent mechanism. Biochem. Biophys. Res. Commun. 388, 311–316.

Owen, M.R., Doran, E., and Halestrap, A.P. (2000). Evidence that metformin exerts its anti-diabetic effects through inhibition of complex 1 of the mitochondrial respiratory chain. Biochem. J. 348, 607–614.

Paik, M.J., Cho, E.Y., Kim, H., Kim, K.R., Choi, S., Ahn, Y.H., and Lee, G. (2008). Simultaneous clinical monitoring of lactic acid, pyruvic acid and ketone bodies in plasma as methoxime/tert-butyldimethylsilyl derivatives by gas chromatography-mass spectrometry in selected ion monitoring mode. Biomed. Chromatogr. 22, 450–453.

Petersen, M.C., Vatner, D.F., and Shulman, G.I. (2017). Regulation of hepatic glucose metabolism in health and disease. Nat. Rev. Endocrinol. 13, 572–587.

Plaisant, M., Giorgetti-Peraldi, S., Gabrielson, M., Loubat, A., Dani, C., and Peraldi, P. (2011). Inhibition of hedgehog signaling decreases proliferation and clonogenicity of human mesenchymal stem cells. PLoS ONE 6, e16798.

Pollak, M. (2012). The insulin and insulin-like growth factor receptor family in neoplasia: an update. Nat. Rev. Cancer 12, 159–169.

Pollak, M. (2013). Potential applications for biguanides in oncology. J. Clin. Invest. 123, 3693–3700.

Rena, G., Hardie, D.G., and Pearson, E.R. (2017). The mechanisms of action of metformin. Diabetologia 60, 1577–1585.

Rosilio, C., Lounnas, N., Nebout, M., Imbert, V., Hagenbeek, T., Spits, H., Asnafi, V., Pontier-Bres, R., Reverso, J., Michiels, J.F., et al. (2013). The metabolic perturbators metformin, phenformin and AICAR interfere with the growth and survival of murine PTEN-deficient T cell lymphomas and human T-ALL/T-LL cancer cells. Cancer Lett. 336, 114–126.

Scheen, A.J. (1996). Clinical pharmacokinetics of metformin. Clin. Pharmacokinet. 30, 359–371.

Segal, E.D., Yasmeen, A., Beauchamp, M.C., Rosenblatt, J., Pollak, M., and Gotlieb, W.H. (2011). Relevance of the OCT1 transporter to the antineoplastic effect of biguanides. Biochem. Biophys. Res. Commun. 414, 694–699.

Seo, B.B., Kitajima-Ihara, T., Chan, E.K., Scheffler, I.E., Matsuno-Yagi, A., and Yagi, T. (1998). Molecular remedy of complex I defects: rotenone-insensitive internal NADH-quinone oxidoreductase of Saccharomyces cerevisiae mitochondria restores the NADH oxidase activity of complex I-deficient mammalian cells. Proc. Natl. Acad. Sci. USA 95, 9167–9171.

Seo, B.B., Matsuno-Yagi, A., and Yagi, T. (1999). Modulation of oxidative phosphorylation of human kidney 293 cells by transfection with the internal rotenone-insensitive NADH-quinone oxidoreductase (NDI1) gene of Saccharomyces cerevisiae. Biochim. Biophys. Acta 1412, 56–65.

Shackelford, D.B., Abt, E., Gerken, L., Vasquez, D.S., Seki, A., Leblanc, M., Wei, L., Fishbein, M.C., Czernin, J., Mischel, P.S., and Shaw, R.J. (2013). LKB1 inactivation dictates therapeutic response of non-small cell lung cancer to the metabolism drug phenformin. Cancer Cell 23, 143–158.

Shaw, R.J. (2009). LKB1 and AMP-activated protein kinase control of mTOR signalling and growth. Acta Physiol. (Oxf.) 196, 65–80.

Shaw, R.J., Lamia, K.A., Vasquez, D., Koo, S.H., Bardeesy, N., Depinho, R.A., Montminy, M., and Cantley, L.C. (2005). The kinase LKB1 mediates glucose homeostasis in liver and therapeutic effects of metformin. Science 310, 1642–1646.

Shen, Y., Kapfhamer, D., Minnella, A.M., Kim, J.E., Won, S.J., Chen, Y., Huang, Y., Low, L.H., Massa, S.M., and Swanson, R.A. (2017). Bioenergetic state regulates innate inflammatory responses through the transcriptional co-repressor CtBP. Nat. Commun. 8, 624.

Steven, A., and Seliger, B. (2016). Control of CREB expression in tumors: from molecular mechanisms and signal transduction pathways to therapeutic target. Oncotarget 7, 35454–35465.

Tang, Y., Gholamin, S., Schubert, S., Willardson, M.I., Lee, A., Bandopadhayay, P., Bergthold, G., Masoud, S., Nguyen, B., Vue, N., et al. (2014). Epigenetic targeting of Hedgehog pathway transcriptional output through BET bromodomain inhibition. Nat. Med. 20, 732–740.

Wang, Y., Ding, Q., Yen, C.J., Xia, W., Izzo, J.G., Lang, J.Y., Li, C.W., Hsu, J.L., Miller, S.A., Wang, X., et al. (2012). The crosstalk of mTOR/S6K1 and Hedgehog pathways. Cancer Cell 21, 374–387.

Wang, Y., An, H., Liu, T., Qin, C., Sesaki, H., Guo, S., Radovick, S., Hussain, M., Maheshwari, A., Wondisford, F.E., et al. (2019). Metformin Improves Mitochondrial Respiratory Activity through Activation of AMPK. Cell Rep. 29, 1511–1523.

Wheaton, W.W., Weinberg, S.E., Hamanaka, R.B., Soberanes, S., Sullivan, L.B., Anso, E., Glasauer, A., Dufour, E., Mutlu, G.M., Budigner, G.S., and Chandel, N.S. (2014). Metformin inhibits mitochondrial complex I of cancer cells to reduce tumorigenesis. eLife 3, e02242.

Yang, Z.J., Ellis, T., Markant, S.L., Read, T.A., Kessler, J.D., Bourboulas, M., Schüller, U., Machold, R., Fishell, G., Rowitch, D.H., et al. (2008). Medulloblastoma can be initiated by deletion of Patched in lineage-restricted progenitors or stem cells. Cancer Cell 14, 135–145.

Zhang, Q., Yao, H., Vo, N., and Goodman, R.H. (2000). Acetylation of adenovirus E1A regulates binding of the transcriptional corepressor CtBP. Proc. Natl. Acad. Sci. USA 97, 14323–14328.

Zhang, Q., Piston, D.W., and Goodman, R.H. (2002). Regulation of corepressor function by nuclear NADH. Science 295, 1895–1897.

Zhang, Q., Wang, S.Y., Nottke, A.C., Rocheleau, J.V., Piston, D.W., and Goodman, R.H. (2006). Redox sensor CtBP mediates hypoxia-induced tumor cell migration. Proc. Natl. Acad. Sci. USA 103, 9029–9033.

Zhao, L.J., Subramanian, T., and Chinnadurai, G. (2006). Changes in C-terminal binding protein 2 (CtBP2) corepressor complex induced by E1A and modulation of E1A transcriptional activity by CtBP2. J. Biol. Chem. 281, 36613–36623.

Zhao, L.J., Kuppuswamy, M., Vijayalingam, S., and Chinnadurai, G. (2009). Interaction of ZEB and histone deacetylase with the PLDLS-binding cleft region of monomeric C-terminal binding protein 2. BMC Mol. Biol. 10, 89.

Zhou, G., Myers, R., Li, Y., Chen, Y., Shen, X., Fenyk-Melody, J., Wu, M., Ventre, J., Doebber, T., Fujii, N., et al. (2001). Role of AMP-activated protein kinase in mechanism of metformin action. J. Clin. Invest. 108, 1167–1174.

STAR★METHODS

KEY RESOURCES TABLE

REAGENT or RESOURCE	SOURCE	IDENTIFIER
Antibodies		
Mouse monoclonal anti-Gli1 (L42B10)	Cell Signaling Technology	Cat# 2643; RRID: AB_2294746
Rabbit polyclonal anti-AMPKα	Cell Signaling Technology	Cat# 2532; RRID: AB_330331
Rabbit monoclonal anti-Phospho-AMPKα(Thr172)(40H9)	Cell Signaling Technology	Cat# 2535; RRID: AB_331250
Rabbit polyclonal anti-CtBP2	Cell Signaling Technology	Cat# 13256; RRID: AB_2798164
Mouse monoclonal anti-CtBP2	BD Biosciences	Cat# 612044; RRID: AB_399431
Mouse monoclonal anti-GPD2 (D-12)	SantaCruz Biotechnology	Cat# sc-390830
Goat polyclonal anti-GPD2 (K-14)	SantaCruz Biotechnology	Cat# sc-161680; RRID: AB_2279181
Mouse monoclonal anti-FLAG M2-Peroxidase (HRP)	Sigma-Aldrich	Cat# A8592; RRID: AB_439702
Mouse monoclonal anti-HA−probe (F7) HRP	SantaCruz Biotechnology	Cat# sc-7392 HRP
Mouse monoclonal anti-Tubulin (TU-02)	SantaCruz Biotechnology	Cat# sc-8035; RRID: AB_628408
Mouse monoclonal anti-Vinculin (7F9)	SantaCruz Biotechnology	Cat# sc-73614; RRID: AB_1131294
Rabbit monoclonal anti-Ki-67	Invitrogen	Cat# MA5-14520; RRID: AB_10979488
Rabbit monoclonal anti-Phospho-4E-BP1(Ser65)(174A9)	Cell Signaling Technology	Cat# 9456; RRID: AB_823413
Rabbit monoclonal anti-4E-BP1(53H11)	Cell Signaling Technology	Cat# 9644; RRID: AB_2097841
Rabbit polyclonal anti-Phospho-S6 Ribosomal Protein (Ser240/244)	Cell Signaling Technology	Cat# 2215; RRID: AB_331682
Rabbit monoclonal anti-S6 Ribosomal Protein (5G10)	Cell Signaling Technology	Cat# 2217; RRID: AB_331355
Rabbit policlonal anti-Phospho-CREB	Laboratory of Marc Montminy	N/A
Rabbit polyclonal anti-Cyclin D1 (C-20)	SantaCruz Biotechnology	Cat# sc-717; RRID: AB_631336
Rabbit polyclonal anti-Cyclin A (H-432)	SantaCruz Biotechnology	Cat# sc-751; RRID: AB_631329
Mouse monoclonal anti-Cyclin E (E-4)	SantaCruz Biotechnology	Cat# sc-25303; RRID: AB_2070958
Mouse monoclonal anti-p21 (187)	SantaCruz Biotechnology	Cat# sc-817; RRID: AB_628072
Rabbit monoclonal anti-SUFU (C81H7)	Cell Signaling Technology	Cat# 2522; RRID: AB_2302728
Mouse monoclonal anti-Actin (C-2)	SantaCruz Biotechnology	Cat# sc-8432; RRID: AB_626630
Rabbit polyclonal anti-Gli1 (H-300)	SantaCruz Biotechnology	Cat# sc-20687; RRID: AB_2111764
Rabbit polyclonal anti-Phospho-Acetyl-CoA Carboxylase (Ser79)	Cell Signaling Technology	Cat# 3661; RRID: AB_330337
Rabbit polyclonal anti-Acetyl-CoA Carboxylase	Cell Signaling Technology	Cat# 3662; RRID: AB_2219400
Rabbit polyclonal anti-Phospho-Raptor (Ser792)	Cell Signaling Technology	Cat# 2083; RRID: AB_2249475
Rabbit monoclonal anti-Raptor (24C12)	Cell Signaling Technology	Cat# 2280; RRID: AB_561245
Rabbit monoclonal anti-Phospho-AMPK Substrate Motif [LXRXX(pS/pT) MultiMab	Cell Signaling Technology	Cat# 5759; RRID: AB_10949320
Mouse monoclonal anti-c-Myc (9E10) HRP	SantaCruz Biotechnology	Cat# sc-40 HRP; RRID: AB_627268
Rabbit polyclonal anti-HDAC2 (H-54)	SantaCruz Biotechnology	Cat# sc-7899; RRID: AB_2118563
Rabbit polyclonal anti-Glucose Transporter GLUT1	Abcam	Cat# ab652; RRID: AB_305540
Chemicals, Peptides, and Recombinant Proteins		
Dulbecco's modified Eagle medium	Sigma-Aldrich	Cat# 6546
DMEM, no glucose	GIBCO	Cat# 11966025
Penicillin-Streptomycin	Sigma-Aldrich	Cat# P0781
L-Glutamine solution	Sigma-Aldrich	Cat# G7513
SAG	AdipoGen Life Sciences	Cat# AG-CR1-3506
D-Glucose solution	Sigma-Aldrich	Cat# G8644
Phenformin hydrochloride	Sigma-Aldrich	Cat# P7045
1,1-Dimethylbiguanide hydrochloride	Sigma-Aldrich	Cat# D150959

(Continued on next page)

Continued

REAGENT or RESOURCE	SOURCE	IDENTIFIER
Rotenone	Sigma-Aldrich	Cat# R8875
Mitochondrial GPDH Inhibitor, iGP-1	Calbiochem	Cat# 530655
Sodium Pyruvate	Sigma-Aldrich	Cat# S8636
Lipofectamine 2000 Transfection Reagent	Invitrogen	Cat# 11668019
Opti-MEM medium	GIBCO	Cat# 31985070
siGENOME Mouse Gli1 siRNA	Dharmacon	Cat# M-047917-01
Neurobasal-A Medium, no D-glucose, no sodium pyruvate	GIBCO	Cat# A2477501
B-27 Supplement (50X), minus vitamin A	GIBCO	Cat# 12587010
Polybrene	Sigma-Aldrich	Cat# H9268
Blasticidine-S-hydrochloride	Sigma-Aldrich	Cat# 15205
Puromycin dihydrochloride from *Streptomyces alboniger*	Sigma-Aldrich	Cat# P8833
Piperacillin	Sigma-Aldrich	Cat# BP1027
Seahorse XF base medium, without phenol red	Agilent	Cat# 103335-100
2,6-Dichloroindophenol sodium salt hydrate	Sigma-Aldrich	Cat# D1878
Critical Commercial Assays		
Firefly & Renilla Luciferase Single Tube Assay Kit	Biotium	Cat# 30081-1
WesternBright ECL HRP Substrate	Advansta	Cat# K-12045-D50
SensiFAST cDNA synthesis kit	Bioline	Cat# BIO-65054
SensiFAST Sybr Lo-Rox Mix	Bioline	Cat# BIO-94020
Seahorse XF Cell Mito Stress Test Kit	Agilent	Cat# 103015-100
EnzyChrom NAD/NADH Assay Kit	BioAssay Systems	Cat# E2ND-100
CellTiter-Glo Luminescent Cell Viability Assay	Promega	Cat# G7571
Glycerol-3-Phosphate Colorimetric Assay Kit	Sigma-Aldrich	Cat# MAK207
Mitochondria/Cytosol Fractionation Kit	Biovision	Cat# K256-100
Experimental Models: Cell Lines		
Human: DAOY cells	ATCC	HTB-186
Mouse: Med1-MB cells	Laboratory of Yoon-Jae Cho	N/A
Experimental Models: Organisms/Strains		
Mouse: C57BL/6J	The Jackson Laboratory	Stock# 000664; RRID: SCR_004894
Mouse: Crl:CD1-*Foxn1*^{nu}	Charles River Laboratories	Strain# 086; RRID: IMSR_CRL:086
Mouse: NOD.CB17-*Prkdc*^{scid}/J	Charles River Laboratories	Strain# 634; RRID: IMSR_JAX:001303
Mouse: Math1-CRE;Ptch1$^{loxP/loxP}$	Laboratory of Robert Wechsler-Reya	N/A
Oligonucleotides		
Oligonucleotide: sh-mGPD Forward - CCGGGCAGAGGTGAAATACGGCATTT CTAGAAATGCCGTATTTCACCTCTGCTTG	This paper	N/A
Oligonucleotide: sh-mGPD Reverse – AATTCAAAAAGCAGAGGTGAAATACGGC ATTTCTAGAAATGCCGTATTTCACCTCTGC	This paper	N/A
Oligonucleotide: shCtBP2 Forward - CCGGTACGAAACTGTGTCAACAAAGT CTAGACTTTGTTGACACAGTTTCGTATTATTG	This paper	N/A
Oligonucleotide: shCtBP2 Reverse - AATTCAAAAATACGAAACTGTGTCAACAA AGTCTAGACTTTGTTGACACAGTTTCGTA	This paper	N/A
Oligonucleotides for AMPKα2, cGPD, NDUFS3, see Table S1	This paper	N/A
Primer: *mGpd* Forward - TGCGCGGTGCAAGGAT	This paper	N/A
Primer: *mGpd* Reverse - GCATTTGGCTCTCACGTCAA	This paper	N/A

(*Continued on next page*)

Continued

REAGENT or RESOURCE	SOURCE	IDENTIFIER
Primer: *Ctbp2* Forward - TTTGTGAAGGTATCCGCCC	This paper	N/A
Primer: *Ctbp2* Reverse - GGTACATCATGGCACCCACA	This paper	N/A
Primers for *mL32*, *hL32*, *mGli1*, *hGli1*, *cGpd*, *Ptch1*, *CyclinD2*, *Ptch1* promoter, *Hprt* control, *Ndi1*, *Ndufs3*, *Eno1*, *Gapdh*, *Pkm*, *Slc2a1*, *Tpi1*, see Table S2	This paper	N/A
Recombinant DNA		
HA-CtBP1	Laboratory of Ulupi Jhala	N/A
FLAG-Myc-CtBP2	Origene	Cat# TP324861
PMXS-NDI1	Birsoy et al., 2014	Addgene Plasmid #72876; RRID: Addgene_72876
AMPKα1 MISSION shRNA	Sigma-Aldrich	TRC number: TRCN0000360841
SUFU MISSION shRNA	Sigma-Aldrich	TRC number: TRCN0000019464
MISSION pLKO.1-puro	Sigma-Aldrich	Cat# SHC002
Software and Algorithms		
ImageJ	NIH	https://imagej.nih.gov/ij/download.html; RRID: SCR_003070
ChemStation	Agilent	https://www.agilent.com/en/products/software-informatics/massspec-workstations/gc-msd-chemstation-software; RRID: SCR_015742
Prism v.6.0	GraphPad	https://www.graphpad.com/scientific-software/prism/; RRID: SCR_002798
Other		
Seahorse XFe96, FluxPak mini	Agilent	Cat# 102601-100
Protran Nitrocellulose Hybridization Transfer Membrane	Perkin Elmer	Cat# NBA085C001EA
Kinetex Biphenyl LC Column (150x4.6 mm; 5 μm particle size)	Phenomenex	Cat# 00F-4627-E0
HP-5ms fused-silica capillary column (30mx0.25 mm i.d.)	Agilent J&W	Cat# 19091S-433E

LEAD CONTACT AND MATERIALS AVAILABILITY

Further information and request for resources and reagents should be directed to and will be fulfilled by the Lead Contact, Gianluca Canettieri (gianluca.canettieri@uniroma1.it). All unique/stable reagents generated in this study are available from the Lead Contact with a completed Materials Transfer Agreement.

EXPERIMENTAL MODEL AND SUBJECT DETAILS

Cell lines and cultures

Med1-MB cells (kindly provided by Yoon-Jae Cho (Stanford, CA USA)) were obtained from a medulloblastoma spontaneously originated in Ptch^{+/−};lacZ mouse (Hayden Gephart et al., 2013; Tang et al., 2014) carrying a monoallelic inactivation of the inhibitory receptor *Patched1* gene, resulting in the constitutive activation of Hh pathway (Goodrich et al., 1997). These cells were, cultured in Dulbecco's modified Eagle medium (DMEM) supplemented with 10% FBS, 1 mM penicillin-streptomycin and 1 mM glutamine. MB cultures were derived from spontaneous, intracranial MB from Math1-CRE;Ptch1[loxP/loxP] mice. Tumors were harvested, dissociated and cultured as previously described (Di Magno et al., 2014). DAOY cells were obtained from ATCC (ATCC® HTB-186™) and cultured as previously described (Coni et al., 2017; D'Amico et al., 2015; Di Magno et al., 2016). All cells were cultured in a humidified incubator at 37°C and 5% CO_2. For SAG treatment, DAOY cells were incubated overnight in serum-free medium containing 0.5% BSA and glucose 0.75 mM and the exposed to SAG (200 nM, #AG-CR1-3506, AdipoGen Life Sciences) for 48 hours. ASZ001 and TC-71 cell lines were cultured as previously described (D'Amico et al., 2015; Infante et al., 2015). Phenformin (#P7045), metformin (#D150959) and rotenone (#R8875) were purchased from Sigma-Aldrich, mitochondrial GPD inhibitor iGP-1 (#530655) was purchased from Calbiochem and dissolved in DMSO. Treatments were performed in DMEM no glucose, no sodium pyruvate (#11966025, GIBCO) supplemented with 10% FBS, 1mM penicillin-streptomycin, 1mM glutamine and glucose (25 mM or 5.5 mM or 0.75 mM, as indicated in the text).

In vivo mouse studies

Math1-CRE;Ptch1$^{loxP/loxP}$ mice were previously described (Yang et al., 2008). C57BL/6J mice were obtained from The Jackson Laboratory (Bar Harbor, ME, USA). CD1-nude mice and NOD/SCID mice were purchased from Charles Rives Laboratories (Calco, LE, Italy). All animals were housed with 12 hours light/darkness and standard chow diet at 23°C.

For the Kaplan Meier analysis (Figure 1H), female Math1-CRE;Ptch1$^{loxP/loxP}$ mice were divided into two treatment groups (n = 8): 1) non treated control group and 2) group treated with phenformin at a concentration of 300mg/Kg/day, administered through the drinking water (Appleyard et al., 2012). The treatment started when mice where 35 days old. The survival rate over time was estimated as the number of life days from the start of pharmacological treatment. For short-term treatments (Figures 1C, 1F, 2F, and 6E; Figures S2C, S2D, S3C, and S3D; scheme in Figure S1C), mice were i.v. injected with PBS or phenformin and were euthanized at 0.5, 1, 2 and 4 hours post-injection, or treated with phenformin by o.p. (Figure 1B) and euthanized at 0.5, 1 and 2 hours post-treatment. Long-term treatments consisted of 10 days (Figure 1D; Figure S1C) to four weeks (Figures 1E, 1I, 3E, 3H, and 6; Figures S2F and S2J) treatment with *ad libitum* phenformin (300 mg/Kg/day) in the drinking water, or 5 to 7 days treatment (Figures 1G, 2C, and 4B; Figures S1C and S4B) with phenformin (200 mg/Kg) via o.p. once a day.

Tumor allograft experiments were performed as previously described (Di Magno et al., 2014). Four weeks old female NOD/SCID and CD1-nude mice were injected on each flank with 2 x 10^6 medulloblastoma cells deriving from Math1-CRE;Ptch1$^{loxP/loxP}$ mice, or with 2 x 10^6 Med1-MB cells stably expressing shRNA-Control or shRNA-CtBP2. Tumors were grown until they reached 100 mm^3 volume. Animals were randomly divided into two groups (n = 5) and administered with vehicle (water) or phenformin (300 mg/Kg/day) in the drinking water (Appleyard et al., 2012).

For mouse experiments with NDI1-expressing MB cells, 2 × 10^6 Control-Med1-MB or NDI1-Med1-MB cells were injected into the right and left flanks of 4 weeks old female NOD/SCID mice. When the tumors reached 100 mm^3 volumes, mice were randomly divided into 4 experimental groups: Control-Med1-MB treated with (n = 5) or without phenformin (300 mg/Kg) (n = 5), NDI1-Med1-MB treated with (n = 5) or without phenformin (300 mg/Kg) (n = 5). Phenformin was delivered in drinking water.

Tumor volumes were measured with a caliper, using the following formula: V = (L x W^2)/2 (Kim et al., 2013). All animal experiments were approved by local ethics authorities.

METHOD DETAILS

Transfections and luciferase assays

Med1-MB cells were transfected with Lipofectamine 2000 (3 μl/μg of DNA, #11668019, Invitrogen) in Opti-MEM medium (#31985070, GIBCO). For luciferase assays, Med1-MB cells were seeded and transfected with siRNA against Gli1 (100 nM, #M-047917-01, Dharmacon) using Lipofectamine 2000 for 48 hours. After siRNA transfection, cells were re-seeded in 12-well plates and transfected with the 12xGli-Luc luciferase reporter (50 ng), TK-renilla plasmid (10 ng) and FLAG-CtBP2 or FLAG-pcDNA3 (440 ng) expression vectors, using Lipofectamine 2000 for 48 hours. Luciferase reporter assay was performed with the Firefly and Renilla Luciferase Single Tube Assay Kit (#30081-1, Biotium). Relative luciferase activity is expressed as the ratio of luciferase and renilla activity in control and Gli1 knockdown cells expressing FLAG-CtBP2 or FLAG-pcDNA3 plasmids.

Determination of cell proliferation and tumorspheres size

2 × 10^4 Med1-MB cells were seeded in 12-well plate and incubated overnight at 37°C. After 24 hours from seeding, cells were treated with phenformin or metformin at the concentrations indicated in the text. Every 24 hours cells were trypsinized and counted by trypan blue exclusion method.

Tumorspheres diameters were measured using ImageJ software (Rasband, W.S., ImageJ, U. S. National Institutes of Health, Bethesda, Maryland, USA, https://imagej.nih.gov/ij/, 1997-2018). Briefly, tumorspheres were seeded in Neurobasal-A medium no D-glucose (#A2477501, GIBCO) supplemented with B-27 supplement minus vitamin A (#12587010, GIBCO), 1mM penicillin-streptomycin, 1mM glutamine and 0.75mM glucose and treated with phenformin (5 μM) for 48 hours. After incubation, tumorspheres images were captured under an inverted microscope and diameters were measured.

Western blotting, immunoprecipitation and phosphorylation assays

Cells or tissues were collected at the end of the treatments and lysed in denaturing buffer containing 50 mM Tris-HCl, 2% SDS, 10% Glycerol, 10 mM Na4P2O7, 100 mM NaF, 6 M Urea, 10 mM EDTA. Protein extracts were quantified and resolved by SDS–polyacrylamide gel electrophoresis and transferred to a nitrocellulose membrane (#NBA085C001EA, Perkin Elmer). After blocking, membranes were incubated with primary antibodies overnight and HPR-conjugated secondary antibodies. Detection of the horseradish peroxidase signal was performed using WesternBright ECL (#K-12045-D50, Advansta), according to the manufacturer's protocol. Signal intensity was quantified by ImageJ software. Immunoprecipitation and phosphorylation assays were performed as previously described (Canettieri et al., 2010; Di Magno et al., 2016).

Plasmids and antibodies

HA-CtBP1 plasmid was a gift from Dr. Ulupi Jhala (PDRC, CA USA). FLAG-Myc-CtBP2 was purchased from Origene (#TP324861). PCDNA3FLAG-Gli1, 12xGli-Luc, TK-renilla, FLAG-pcDNA3, Myc-GLI2 and FLAG-GLI3 were previously described (Canettieri et al.,

2009, 2010). PMXS-NDI1 was a gift from David Sabatini (Birsoy et al., 2014) (Addgene plasmid #72876; http://www.addgene.org/72876/; RRID:Addgene_72876). The following antibodies were used: Gli1 (#2643 Cell Signaling, WB 1:1000), AMPKα (#2532 Cell Signaling WB 1:1000), phospho-AMPKα (#2535 Cell Signaling, WB 1:1000), CtBP2 (#13256 Cell Signaling, WB 1:1000), CtBP2 (#612044 BD Biosciences, ChIP 1:1000), GPD2 (D-12) (#sc-390830 SantaCruz Biotechnology, WB 1:500), GPD2 (K-14) (#sc-161680 SantaCruz Biotechnology, WB 1:1000), FLAG-HRP (#A8592 Sigma-Aldrich, WB 1:10000), HA-HRP (#sc-7392 HRP Santa-Cruz Biotechnology, WB 1:10000), Tubulin (#sc-8035 SantaCruz Biotechnology, WB 1:1000), Vinculin (#sc-73614 SantaCruz Biotechnology, WB 1:1000), Ki-67 (#MA5-14520 Invitrogen, IHC 1:100), phospho-4E-BP1 (#9456 Cell Signaling, WB 1:1000), 4E-BP1 (#9644 Cell Signaling, WB 1:1000), phospho-S6 Ribosomal Protein (#2215 Cell Signaling, WB 1:1000), S6 Ribosomal Protein (#2217 Cell Signaling, WB 1:1000), phospho-CREB (from Dr. Marc Montminy's laboratory, Salk Institute, WB 1:2000), Cyclin D1 (#sc-717 SantaCruz Biotechnology, WB 1:1000), Cyclin A (#sc-751 SantaCruz Biotechnology, WB 1:1000), Cyclin E (#sc-25303 SantaCruz Biotechnology, WB 1:1000), p21 (#sc-817 SantaCruz Biotechnology, WB 1:1000), SuFu (#2522 Cell Signaling, WB 1:1000), Actin (#sc-8432 SantaCruz Biotechnology, WB 1:1000), Gli1 (H-300) (#sc-20687 SantaCruz Biotechnology, IHC 1:200), phospho-ACC (#3661 Cell Signaling, WB 1:1000), ACC (#3662 Cell Signaling, WB 1:1000), phospho-Raptor (#2083 Cell Signaling, WB 1:1000), Raptor (#2280 Cell Signaling, WB 1:1000), phospho-(Ser/Thr) AMPK Substrate (#5759, Cell signaling, 1:1000), c-Myc-HRP (#sc-40 HRP SantaCruz Biotechnology, WB 1:5000), HDAC2 (#sc-7899 SantaCruz Biotechnology, WB 1:1000), GLUT1 (#ab652 Abcam, WB 1:1000).

Lentiviral-mediated shRNA knockdown and retroviral delivery

shRNA knockdown was performed through lentiviral infection. HEK293 cells were transfected by calcium phosphate precipitation with 20 μg of different pLKO.1 vectors (Sigma-Aldrich) together with 15 μg of pCMV-R 8.74, and 10 μg of pMDG, to produce lenti-viruses. After 24 hours, the medium was changed and supernatant containing recombinant lentiviruses was collected 48 and 72 hours after transfection. AMPKα1 (TRCN0000360841), SuFu (TRCN0000019464) and control shRNA (scrambled, #SHC002) were obtained by Sigma-Aldrich. PLKO.1 vector expressing shRNA directed against AMPKα2, cGPD, mGPD and CtBP2 were cloned in PLKO.1 TCR vector with the oligos listed in Table S1. Virus titers were determined using quantitative real-time PCR as previously described (Barczak et al., 2015). To perform lentiviral transduction, Med1-MB cells were seeded overnight in 60mm plates. The day after, 5 MOI of lentivirus were complexed with 5 μg/ml polybrene (#H9268, Sigma-Aldrich), added to the cells and left 24 hours before being removed and replaced with standard medium. Knockdown efficiency was monitored by western blotting and/or qPCR.

For retroviral packaging, 2.5×10^6 Phoenix cells were seeded in 100 mm cell culture dishes. 24 hours after plating, cells were transfected with 20 μg PMXS-NDI1 or control vectors, using $CaCl_2$ precipitation. After 20 hours, medium was replaced with fresh medium and supernatant containing recombinant retroviruses was collected 48 hours after transfection. For retroviral infection, Med1-MB cells were seeded at subconfluence and incubated with retroviral supernatant containing polybrene (5 μg/ml). The infection was repeated three times at 12 hours intervals. Control-Med1-MB and NDI1-Med1-MB cells were isolated through antibiotic selection (blasticidine-S-hydrochloride, #15205, Sigma-Aldrich, 2 μg/ml) for 7 days. Monoclonal cell lines were obtained by limiting dilution.

shRNA-mediated NDUFS3 knockdown was obtained through lentiviral infection. Control-Med1-MB and NDI1-Med1-MB cells were infected with control (shCtrl) or NDUFS3-specific shRNA and selected by puromycin (#P8833, Sigma-Aldrich, 5 μg/ml).

Quantitative Real-Time PCR (qPCR) assay

Total mRNA was isolated from cells as previously described (Canettieri et al., 2010; Antonucci et al., 2014). Complementary DNA (cDNA) was synthesized by the Sensifast cDNA synthesis kit (#BIO-65054, Bioline). Quantitative PCR was performed with SensiFast Sybr Lo-Rox Mix (#BIO-94020, Bioline), and transcript levels were quantified with the Applied Biosystems ViiA 7 Real-Time PCR System instrument. Each sample was normalized on *L32* mRNA levels. Primer sequences are listed in Table S2.

Chromatin immunoprecipitation (ChIP) assay

Chromatin immunoprecipitation experiments were performed as described previously (Canettieri et al., 2010). Mouse polyclonal anti-CtBP2 (#612044, BD Biosciences) antibody was used to precipitate endogenous CtBP2. Eluted DNA was PCR-amplified with primers encompassing the *Ptch1* promoter or *Hprt* gene as internal control.

Immunohistochemistry (IHC)

Immunohistochemical analysis of allografted tumor sections was performed as described (Coni et al., 2013). The following antibodies and conditions were used: Ki-67 was diluted in PBS-T containing 1% serum, Gli1 (H300) was diluted in PBS-T containing 5% serum. Antibodies were incubated for one hour at room temperature. Nuclei were counterstained with hematoxylin in accordance with standard procedures.

Determination of phenformin concentration

All chemicals were of analytical grade, readily available commercial products and were obtained from Sigma-Aldrich (San Louis, MO, USA). The HPLC-system was an Agilent Technologies 1200 Series equipped with a variable wavelength detector (VWD) operating at a wavelength of 240 nm. All the operations, such as the injection cycle, were controlled by the ChemStation program; the data obtained were analyzed with the ChemStation program (Agilent Technologies Deutschland GmbH, Waldbronn, Germany). Stock

standard solutions of phenformin were prepared by dissolving 10 mg of analyte in 10 mL of water/methanol (50/50) to make a standard solution of 1 mg/mL. Piperacillin internal standard stock solution was prepared by dissolving 10 mg piperacillin in 10 mL of water to obtain a concentration of 1 mg/mL. The stock standards and internal standard solutions were aliquoted (200 µL) and stored at -80°C until use. Calibration samples of phenformin (30-10000 ng/mL) and internal standard (200 µg/mL) were prepared by adding varying volumes of standard stock solutions and fixed volume of internal standard stock solution into pooled drug-free plasma. The peak area ratio of phenformin to internal standard was measured, and a calibration curve was obtained from the least-squares linear regression of the peak area ratio with spiked concentrations.

The extraction procedure and HPLC analysis has been performed, with changes, as reported by Cheng and Chou (2001). Briefly, up to 200 µL of blood samples were collected into a 0.2 mL capillary tube and transferred into micro-tubes, both containing sprayed EDTA, and immediately centrifuged. The plasma was stored at −80°C. Tissues sample were collected into 1 mL tubes, sonicated and stored at −80°C. Samples were prepared as follows: sample (100 µL) was spiked with 10 µL of the internal standard solution (piperacillin 200 µg/mL) and 10 µL of 1M HCl. After vortexing for 30 s, the mixture was extracted with 300 µL of acetonitrile by vortex for 30 s, and then centrifuged at 13,000 rpm for 9 minutes. The organic phase was separated and evaporated to dryness at 30°C and under a nitrogen stream. The extracts were reconstituted with 100 µL of water and washed with 150 µL of dichloromethane by vortex for 30 s. After centrifugation at 13,000 rpm for 9 minutes, 60 µL of aqueous layer was injected into a Kinetex Biphenyl LC column (150x4.6 mm; 5 µm particle size; Phenomenex). Phenformin was isocratically eluted from the column using mobile phase acetonitrile:phosphate buffer 30 mM pH 7.0, 25:75, v/v.

Retention time of phenformin was 2.715 minutes at 30°C and a flow rate of 1 mL/min. Total HPLC run time was 5 minutes; re-equilibration time was 0.3 minutes. The concentrations of phenformin were calculated according to the peak area and were compared both with piperacillin as internal standard and with reference curves constructed with escalating concentration of phenformin (30 to 10000 ng/mL).

Metabolic assays

Real time bioenergetics analysis of oxygen consumption rate (OCR) was performed using the XF^e-96 Extracellular Flux Analyzer (Seahorse Bioscience). Cells were seeded at a density of 4×10^3 cells/well in XF^e-96 plates (Seahorse Bioscience) and cultured in 200 µL Dulbecco's modified Eagle's medium containing 25 mM glucose and 1mM glutamine for 24hr and treated with the indicated drugs for 6, 24 and 48 hours in DMEM containing 0.75 mM glucose. Wells were washed and cells were incubated in a CO_2-free incubator to allow equilibration prior to loading into the XF-96 apparatus. OCR was measured in XF medium (non-buffered DMEM medium containing 0.75 mM glucose and 1 mM glutamine). Perturbation profiling of the use of metabolic pathways was achieved using the Seahorse XF Cell Mito Stress Test Kit (#103015-100, Agilent). The assay conditions in the Seahorse experiments were: 3 min of mixture; 3 min of waiting; and 3 min of measurement.

Total cellular NADH and tissutal NADH were determined using the EnzyChrom NAD/NADH Assay Kit (#E2ND-100, BioAssay Systems) and following manufacturer's instructions. Briefly, 1×10^5 cells or 20 mg of tissue were harvested and homogenized in 100 µL NADH extraction buffer. After incubation at 60°C, samples were neutralized adding 100 µL NAD extraction buffer and 20 µL Assay buffer. Sample were briefly vortexed and spinned down to remove cellular debris. The supernatant was used for NADH measurement with OD at 565 nm using a spectrophotometer. Values were corrected for dilutions and protein content or weight of the samples.

Total cellular ATP and tissue ATP were determined using the CellTiter-Glo Luminescent Cell Viability Assay (#G7571, Promega). Briefly, Med1-MB cells were seeded into 96-well plates (4×10^3 cells per well) and incubated for 24 hours. After incubation, cells were treated with phenformin for 6, 24 and 48 hours. For tissue samples, ATP was extracted as previously described (Chida et al., 2012). The luminescence assay was performed according to the manufacturer's instructions.

Glycerol-3-phosphate was measured using the Glycerol-3-Phosphate Colorimetric Assay Kit (#MAK207, Sigma-Aldrich), following manufacturer's reccomandations. Briefly, 1×10^6 cells or 10 mg of tissue sample were harvested and homogenized in 100 µL of G3P assay buffer. After incubation on ice for 10 minutes, samples were centrifuged to remove insoluble materials. 40 µL of the supernatant were used for glycerol-3-phosphate measurement with OD at 450 nm using a microplate reader. The amount of glycerol-3-phosphate (nmol/well) was extrapolated from a glycerol-3-phosphate standard curve. Values were normalized by protein content or weight of the samples.

Analysis of metabolites by GC-MS

Lactic acid and pyruvic acid were analyzed as methoxime/tertbutyldimethylsilyl derivatives as previously described (Paik et al., 2008). Briefly, cells were collected by centrifugation at 1000 rpm for 5 minutes. 20 µL of supernatant were deproteinized by adding 100 µL of acetonitrile and vortexed for 3 minutes. The mixtures were diluted 1:10 with distilled water and centrifuged at 15,000 rpm for 15 minutes at 4°C to pellet proteins. The deproteinized supernatant was used to quantify extracellular L-lactate by GC-SIM-MS analysis. Aliquots of 0.25 mL of the supernatant layer spiked with the internal standard (IS) 3,4-dimethoxybenzoyc acid (final concentration 1000 ng ml^{-1}) were added to 0.7 mL of distilled water and adjusted to pH $\geq$ 13 with 7 M NaOH. Methoxymation was performed by adding to the reaction mix methoxyamine hydrochloride (5 mg) at 60°C for 60 min. The samples were then washed with diethylether (3 mL x 2) and the aqueous phase was adjusted to pH < 2 with concentrated sulfuric acid. The mixture was saturated with NaCl and extracted with diethyl ether (3 ml) and ethyl acetate (2 ml). The organic extracts were combined in the presence of triethylamine (10 µl) and dried under reduced pressure. The samples were then suspended in 30 µL of toluene subjected to the second

derivatization step by adding 20 mL of MTBSTFA (65°C for 30 min) and analyzed by GC-MS. Results were normalized on cell number and expressed as fold change relative to control samples.

Cerebellum samples were homogenized in a ice-bath using an ultra-turrax T8 blender with the addition of 1mL water:acetonitrile (9:1). The homogenized tissue was centrifuged at 13,000 g for 15 minutes at 4°C. 0.25 mL of the cerebellum extract were spiked with internal standard (IS) 3,4-dimethoxybenzoyc acid (final concentration 1000 ng mL^{-1}) and subjected to methoxymation/ tertbutyldimethylsilylation as described above. Results were normalized by tissue weight and expressed as fold change relative to control samples.

GC-M analyses were performed with an Agilent 6850A gas chromatograph coupled to a 5973N quadrupole mass selective detector (Agilent Technologies, Palo Alto, CA, USA). Chromatographic separations were carried out with an Agilent HP5ms fused-silica capillary column (30 m x 0.25 mm i.d.) coated with 5% phenyl-95%-dimethylpolysiloxane (film thickness 0.25 μm) as stationary phase. Injection mode: splitless at a temperature of 280°C. Column temperature program: 70°C (1 min) then to 300°C at a rate of 20°C/min and held for 10 min. The carrier gas was helium at a constant flow of 1.0 mL/min. The spectra were obtained in the electron impact mode at 70 eV ionization energy; ion source 280°C; ion source vacuum 10^{-5} Torr. MS analysis was performed simultaneously in TIC (mass range scan from m/z 50 to 600 at a rate of 0.42 scans s^{-1}) and SIM mode. GC-SIM-MS analysis was performed selecting the following ions: m/z 174 for pyruvate, m/z 261 for lactate and m/z 239 for 3,4-dimethoxybenzoic acid (internal standard).

mGPD activity assay

Mithocondria were isolated from medulloblastoma or liver from Math1-CRE;Ptch1$^{loxP/loxP}$ mice using Mitochondria/Cytosol fractionation kit (#K256-100, Biovision) and following the manufacturer's protocol. Briefly, tissue samples (20 mg) were homogenized in an ice-cold dounce tissue grinder in 1X Cytosol Extraction Buffer mix. Homogenate was centrifuged 10 minutes at 700 g at 4°C to remove debris and the supernatant was centrifuged again at 10,000 g for 30 minutes at 4°C to isolate mitochondria. mGPD was purified from 1 mg of mitochondrial lysate by immunoprecipitation with anti-mGPD (D-12) antibody (10 μL/sample). mGPD activity assay was performed as previously described (Madiraju et al., 2018). Immunoprecipitates were incubated with or without biguanides for 10 minutes at 37°C, and activity assay was conducted using 2,6-dichloroindophenol (DCIP) as electron acceptor at 38°C. Activity was calculated as loss of absorbance at 600 nm. Immunoprecipitated mGPD protein levels were assayed by immunoblot with anti-mGPD (K-14) antibody.

NMR metabolomics

For metabolite profiling, 2×10^7 Med1-MB cells expressing control or mGPD-specific shRNAs were cultured in media containing 0.75 mM glucose with or without phenformin (5 μM) for 48 hours. Lipid and polar metabolites were extracted using the dual-phase extraction method (Glunde et al., 2005). Briefly, pelleted cells were extracted with ice cold methanol/chloroform/water (1:1:1). After phase separation by centrifugation at 20,000 g at 4°C for 30 min, the polar water–methanol phase containing water soluble cellular metabolites was evaporated using a rotary evaporator and then lyophilized, while the organic phase (lipid phase) was evaporated under nitrogen gas. Both phases of cell extracts were stored at −20°C. High-resolution ^{1}H NMR analyses were performed at 25°C at 400 MHz (9.4 T Bruker AVANCE spectrometer, Karlsruhe, Germany) on aqueous and organic cell extracts using acquisition pulses, water presaturation, data processing and peak area deconvolution as previously described (Canese et al., 2019; Iorio et al., 2010). Quantification of individual metabolites was obtained from peak areas applying the correction factors determined by experiments at the equilibrium of magnetization (90o pulses, 30.00 s interpulse delay). Metabolite quantification was expressed as metabolite percentage relative to total metabolites. All data were calculated as means ± SD and further analyzed using t test.

Correlation analysis between metabolites was performed using nonparametric tests (Spearman's correlation coefficient) by using GraphPad Prism version 6.0. Differences were considered statistically significant at p < 0.05 and further stratified to p < 0.01 and p < 0.001.

QUANTIFICATION AND STATISTICAL ANALYSIS

Statistical analysis was performed using GraphPad Prism version 6.0 for Mac (GraphPad Software, La Jolla, California, USA, https://www.graphpad.com/). Data were analyzed with a paired Student's t test, ANOVA or log-rank test and expressed as mean ± SD p < 0.05 was considered statistically significant. "n" represents the number of cells or mice per group from independent experiments. The statistical details of experiments and the criteria for significance can be found in the figure legends.

DATA AND CODE AVAILABILITY

This study did not generate any unique datasets or code.